

Operational remote sensing of tropospheric aerosol over land from EOS moderate resolution imaging spectroradiometer

Y. J. Kaufman,¹ D. Tanré,² L. A. Remer,³ E. F. Vermote,⁴ A. Chu,³ and B. N. Holben¹

Abstract. Daily distribution of the aerosol optical thickness and columnar mass concentration will be derived over the continents, from the EOS moderate resolution imaging spectroradiometer (MODIS) using dark land targets. Dark land covers are mainly vegetated areas and dark soils observed in the red and blue channels; therefore the method will be limited to the moist parts of the continents (excluding water and ice cover). After the launch of MODIS the distribution of elevated aerosol concentrations, for example, biomass burning in the tropics or urban industrial aerosol in the midlatitudes, will be continuously monitored. The algorithm takes advantage of the MODIS wide spectral range and high spatial resolution and the strong spectral dependence of the aerosol opacity for most aerosol types that result in low optical thickness in the mid-IR (2.1 and 3.8 μm). The main steps of the algorithm are (1) identification of dark pixels in the mid-IR; (2) estimation of their reflectance at 0.47 and 0.66 μm ; and (3) derivation of the optical thickness and mass concentration of the accumulation mode from the detected radiance. To differentiate between dust and aerosol dominated by accumulation mode particles, for example, smoke or sulfates, ratios of the aerosol path radiance at 0.47 and 0.66 μm are used. New dynamic aerosol models for biomass burning aerosol, dust and aerosol from industrial/urban origin, are used to determine the aerosol optical properties used in the algorithm. The error in the retrieved aerosol optical thicknesses, τ_a , is expected to be $\Delta\tau_a = 0.05 \pm 0.2\tau_a$. Daily values are stored on a resolution of 10×10 pixels (1 km nadir resolution). Weighted and gridded 8-day and monthly composites of the optical thickness, the aerosol mass concentration and spectral radiative forcing are generated for selected scattering angles to increase the accuracy. The daily aerosol information over land and oceans [Tanré *et al.*, this issue], combined with continuous aerosol remote sensing from the ground, will be used to study aerosol climatology, to monitor the sources and sinks of specific aerosol types, and to study the interaction of aerosol with water vapor and clouds and their radiative forcing of climate. The aerosol information will also be used for atmospheric corrections of remotely sensed surface reflectance. In this paper, examples of applications and validations are provided.

Introduction

Daily remote sensing of aerosol from satellites over the land and ocean is essential to obtain the global aerosol budget to estimate the contribution of anthropogenic emission to the aerosol budget and to the aerosol radiative forcing of climate [Charlson *et al.*, 1992; Penner *et al.*, 1992; Kaufman, 1995; Andreae, 1995]. Because of the short lifetime of aerosol particles [Charlson *et al.*, 1992] and the corresponding strong spatial variations in the aerosol concentration, ground-based stations cannot assess trends in the global aerosol budget. They are, though, essential in measuring the physical and optical properties of the vertical column of the ambient aerosol [Nakajima

et al., 1983; Shiobara *et al.*, 1991; Kaufman *et al.*, 1994; Holben *et al.*, 1996; Kaufman and Holben, 1996]. Our strategy of global characterization of aerosol distribution and properties is therefore based on a synergy of satellite analysis of aerosol spatial distribution (optical thickness and mass) over land and ocean and continuous ground-based remote sensing and in situ measurements of aerosol [Prospero and Nees, 1986] from stations distributed over locations that can characterize the properties of aerosol from a variety of ecosystems. The ground-based measurements should validate the satellite remote sensing, add detailed size distribution of the ambient aerosol, used together with the satellite data to monitor the single-scattering albedo [Kaufman, 1987; Wang and Gordon, 1993] and vertical structure (from lidars).

The need for routine monitoring of aerosol is due to the mounting evidence of the importance of aerosol radiative forcing of climate by reflecting sunlight back to space [Joseph, 1984; Tanré *et al.*, 1984; Coakley and Cess, 1985; Charlson *et al.*, 1992; Penner *et al.*, 1992; Kiehl *et al.*, 1993] and its effect on cloud microphysics and albedo [Twomey *et al.*, 1984; Coakley *et al.*, 1987; Kaufman and Nakajima, 1993]. Uncertainty in modeling this forcing is considered one of the largest uncertainties in modeling climate change [Hansen and Lacis, 1990; Intergov-

¹NASA Goddard Space Flight Center, Greenbelt, Maryland.

²Laboratoire d'Optique Atmosphérique, Université de Sciences et Techniques de Lille, Villeneuve d'Ascq, France.

³Science, Systems and Applications Inc., NASA Goddard Space Flight Center, Greenbelt, Maryland.

⁴Department of Geography, University of Maryland, and NASA Goddard Space Flight Center, Greenbelt, Maryland.

This paper is not subject to U.S. copyright. Published in 1997 by the American Geophysical Union.

Paper number 96JD03988.

environmental Panel on Climate Change (IPCC), 1995]. The aerosol forcing is opposite in magnitude to the forcing by greenhouse gases and also has a different spatial distribution and diurnal cycle, thus together generating a complex climatic impact [Karl et al., 1995]. The inclusion of a careful estimate of the sulfate aerosol radiative forcing in climate models resulted in a better fit to the global distribution of measured temperature change [Santer et al., 1996], which boosts our confidence in climate models to predict the warming from greenhouse gases. While industrial/urban aerosol and biomass burning smoke were considered as the main anthropogenic sources of aerosol, recently attention was directed also toward dust originating from changes in land use as a major source of man-induced atmospheric aerosol [Prospero and Nees, 1986; Tegen et al., 1996; Li et al., 1996; Andreae, 1996; Sokolik and Toon, 1996].

Aerosol particles also have an important impact on many biogeochemical processes by serving as the surfaces for speeding chemical reactions. Biomass burning is an important source of organic particles, while the arid and semiarid regions are sources of mineral dust [Prospero, 1981; Pye, 1987]. Aerosol particles also play an important role in tropospheric chemistry by serving as the liquid phase that stimulates chemical reactions [Crutzen, 1983; Taylor et al., 1983]. To fully understand these processes, the aerosol characteristics (spatial and vertical concentration, temporal evolution, size distribution, composition, and optical properties) have to be determined at a global scale. Only an orchestrated approach based on routine analysis of satellite data acquired over land and ocean, together with detailed aerosol characterization derived from ground-based stations with remote sensing and in situ instrumentation, can supply such needed information. Several satellite sensors, planned to be launched in the next several years, are designed to meet these demands (i.e., to measure global distribution of aerosol concentration and properties) using the spectral, angular, or polarization properties of solar radiation that interacted with the aerosol. The use of spectral properties is emphasized by EOS-MODIS [Salomonson et al., 1989; King et al., 1992; Tanré et al., this issue] and by ADEOS-OCTS (ADEOS ocean color and temperature scanner) and GLI (global imager) sensors. The angular characteristics are emphasized by EOS-MISR (multiangle imaging spectroradiometer) [Martonchik and Diner, 1992] and ADEOS-POLDER (polarization and directionality of Earth's reflectances), and the polarization measurements are particularly emphasized by POLDER [Deuzé et al., 1993; Deschamps et al., 1994] and EOS-EOSP (Earth observing scanning polarimeter) [Travis, 1993]. The geostationary satellites (GOES and Meteosat) provide the diurnal cycle of the aerosol spatial distribution [Prins and Menzel, 1994], which is complementary to the polar orbiting satellites. A review of methods for remote sensing of aerosol and their radiative forcing is given by Kaufman [1995], and a collection of papers on this subject can be found in this issue.

Present satellite measurements are limited to reflectance measurements in one channel from geostationary satellite (e.g., GOES or Meteosat) [Fraser et al., 1984] or two channels from polar orbiters (e.g., AVHRR-NOAA) [Kaufman et al., 1990a; Durkee et al., 1991]. Algorithms for retrieving the aerosol component assume an aerosol model for deriving the aerosol optical thickness, which is dependent on the total aerosol content. The aerosol model used is taken from literature as the most representative one of the local conditions [Whitby, 1978; Shettle and Fenn, 1979; D'Almeida et al., 1991]. Such methods have been successfully applied over water [Griggs, 1975, 1979;

Mekler et al., 1977; Koepke and Quenzel, 1979] to produce an operational product from NOAA-AVHRR measurements [Rao et al., 1989; Ignatov et al., 1995]. Most of the remote sensing studies have been devoted to Saharan dust [Fraser, 1976; Carlson, 1979; Norton et al., 1980; Dulac et al., 1992; Jankowiak and Tanré, 1992]. Over the land, so far there has been no real attempt to retrieve aerosol at a global scale. That is because the measured signal is a composite of reflection of sunlight by the variable surface cover and backscattering by the semitransparent aerosol layer, which makes remote sensing of aerosol difficult. Uncertainty and variability in the aerosol size distribution and corresponding scattering phase function generates major errors in the derived aerosol optical thickness [Kaufman and Sendra, 1988, hereinafter referred to as KS88]. Uncertainty in the aerosol absorption properties can introduce additional error but mainly for higher surface reflectance [Fraser and Kaufman, 1985]. An example of variability of the aerosol size is the process that governs sulfate particles. In this process, the sulfate particles are formed by oxidation of SO₂ mainly on existing particles directly, or via cloud processes [Langner et al., 1992; Kaufman and Tanré, 1994], which results in the size of the particles to strongly depend on the relative concentrations of the aerosol particles and SO₂. Despite these difficulties, aerosol should be routinely sensed over the land, not only because most sources of anthropogenic aerosol or its precursor are located over the land but also because it is the place where a big part of the radiative forcing is concentrated [Kiehl and Briegleb, 1993; Jones et al., 1994] and significant climate signal expected [Karl et al., 1995].

The present approach for remote sensing of aerosol over the land from EOS-MODIS is based on detection of aerosol over dark surface covers [Fraser et al., 1984; Fraser and Kaufman, 1985; KS88]. Therefore the algorithm will be applied mainly to the moist parts of the continents. Though it is a serious limitation, these are also the regions where a large part of the human activity takes place. Radiative forcing by aerosol is stronger for low surface albedo; therefore it is important that the algorithm be able to report aerosol loading and forcing over the vegetated parts of the continents, in addition to the oceans [Tanré et al., this issue]. The use of contrasts for highly reflective surface to determine aerosol optical thickness [Tanré et al., 1988] is planned to be introduced into the procedure in a later stage.

Remote Sensing Approach

Basic Strategy

Remote sensing of aerosol stems from the relationship between the measured radiance at the top of the atmosphere ρ^* (given in apparent reflectance units, $\rho^* = \pi L / F_0 \mu_0$, where L is the radiance at the top of the atmosphere, F_0 is the extra-terrestrial solar flux, and μ_0 is the cosine of the solar zenith angle) and the surface bidirectional reflectance properties $\rho(\theta, \theta_0, \phi)$:

$$\rho^*(\theta, \theta_0, \phi) = \rho_a(\theta, \theta_0, \phi) + F_d(\theta_0)T(\theta)\rho(\theta, \theta_0, \phi)/(1 - s\rho') \quad (1)$$

where θ is the view zenith angle, θ_0 is the solar zenith angle, and ϕ is the azimuth of the scattered radiation from the solar beam; $\rho_a(\theta, \theta_0, \phi)$ is the path radiance, $F_d(\theta_0)$ is the normalized downward total flux for zero surface reflectance, equivalent to the total downward transmission. Its value is less than 1.0 due to aerosol and molecular absorption and back-

scattering of sunlight to space. $T(\theta)$ is the upward total transmission into the direction of the satellite field of view; s is the atmospheric backscattering ratio and ρ' is the surface reflectance averaged on the view and illumination angles. The bidirectional reflectance properties of ρ are approximated here by the direct value of the surface reflectance for the illumination and viewing directions and are considered as Lambertian. The error resulting from this approximation is small for dark surfaces used to derive the aerosol path radiance and optical thickness [Lee and Kaufman, 1986].

In the single-scattering approximation used here for illustration of the physical processes involved, the path radiance is proportional to the aerosol optical thickness τ_a , the aerosol scattering phase function $P_a(\theta, \theta_0, \phi)$, and single-scattering albedo ω_0 :

$$\rho_a(\theta, \theta_0, \phi) = \rho_m(\theta, \theta_0, \phi) + \omega_0 \tau_a P_a(\theta, \theta_0, \phi) / (4 \mu \mu_0) \quad (2)$$

where $\rho_m(\theta, \theta_0, \phi)$ is the path radiance due to molecular scattering, μ and μ_0 are cosines of the view and illumination directions, respectively. The functions F_d , T , and s are also dependent on ω_0 , τ_a , and P_a , though for small surface reflectance they are less important. However, in order to derive the aerosol optical thickness from the measured radiance, an aerosol model that provides values of ω_0 and P_a for specific conditions is required.

The contribution to ρ^* from the path radiance is larger for shorter wavelengths and for low values of the surface reflectance (e.g., $\rho \leq 0.06$; see Figure 1). Therefore the errors in deriving the aerosol optical thickness are expected to be smaller in these conditions. Errors due to uncertainty in the aerosol absorption, given by the single-scattering albedo ω_0 are also smaller for low surface reflectance. Thus it is appropriate to use the darkest pixels in the image to estimate the aerosol optical thickness (or loading) and its effect on remote sensing. Independent of surface reflectance, the derivation of optical thickness from the path radiance is also affected by uncertainty in the scattering phase function, which will be discussed later. Many land covers such as vegetation and soils that are dark in the red (0.60–0.68 μm) and blue (0.4–0.48 μm) spectral regions are most suitable for this application. However, in order to use (1) to estimate accurately the path radiance (ρ_a) and the optical thickness, the surface reflectance of these dark pixels have to be estimated within a small uncertainty of $\Delta\rho = \pm 0.005$ to ± 0.01 .

The strategy for remote sensing of aerosol over land from EOS-MODIS is thus based on the following physical principles:

1. Except for dust, the aerosol effect on the radiance measured from space decreases with wavelength as λ^{-1} to λ^{-2} [Kaufman, 1993]. Therefore the effect is much smaller in the mid-IR than in the visible.
2. The radiative effect of aerosol includes backscattering and absorption of the direct sunlight and sunlight reflected from the surface. For dark surfaces the scattering effect dominates, while for brighter surfaces, the effect is mixed. Therefore the aerosol radiative effect is strongest for low surface reflectance. Remote sensing of aerosol using dark targets can be best done for surface reflectance $\rho \leq 0.06$. In this paper, we describe a method to find the surface covers that have this low reflectance in selected wavelengths.
3. The surface reflectance across the solar spectrum is correlated to some extent. Soils usually have an increasing reflectance as a function of the wavelength with correlation between

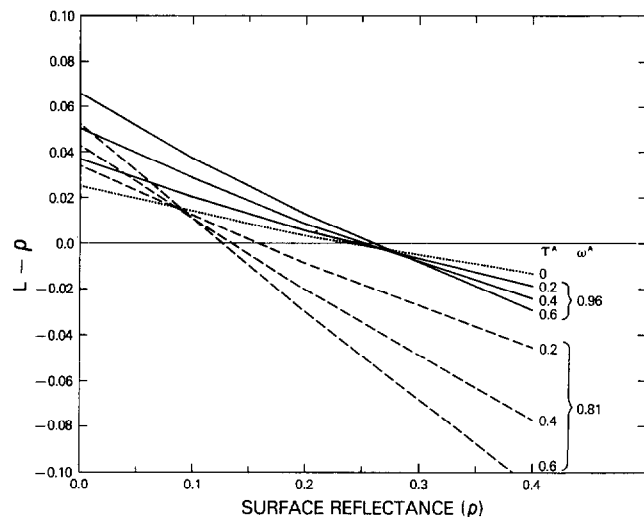


Figure 1. Radiance L at the top of the Earth-atmosphere system (in reflectance units) minus the surface reflectance ρ for nadir observation as a function of the surface reflectance. The total aerosol optical thickness τ_a and the single-scattering albedo ω_0 are indicated for each line. The solar zenith angle is 40° and the wavelength is at $0.61 \mu\text{m}$. Power law size distribution was used with $\nu = 3$. Note that the atmospheric effect is zero for an empty atmosphere ($L - \rho = 0$), and the aerosol effect is zero for the dotted line (pure molecular scattering). For surface reflectance under a given critical value (ρ_c) the aerosol effect is positive ($\rho_c = 0.25$ for $\omega_0 = 0.96$), and above this value the effect is negative [after Fraser and Kaufman, 1985].

the reflectances slowly decreasing with an increase of the wavelength span. Parallel processes affect the reflectance in the 0.47 and 0.66 μm channels and in the 2.1 and 3.8 μm channels. The presence of vegetation decreases the reflectivity in the visible channels due to chlorophyll absorption and in the mid-IR channels due to absorption by liquid water associated with the plant. Wet soil has a lower reflectance in the visible channels due to light-trapping capability and in the 2.1 and 3.8 μm channels due to liquid water absorption. Surface roughness, shadows, and inclinations decrease the reflectance across the whole solar spectrum [Kaufman and Remer, 1994].

On the basis of these principles the basic approach for operational, unsupervised remote sensing of aerosol can be designed as follows: (1) determination of the presence of the dark pixels in the blue (0.47 μm) and red (0.66 μm) channels using their remotely sensed reflectance in the mid-IR channels (2.1 and 3.8 μm); (2) estimation of the surface reflectance of the dark pixels in the red and blue channels using the measurements in the mid-IR; (3) determination of the aerosol type using information on the global aerosol distribution [d'Almeida et al., 1991; Hao and Liu, 1994; Husar et al., this issue] and the ratio between the aerosol path radiance in the red and blue channels; (4) selection of the appropriate dynamical aerosol model [Remer et al., 1996], which describes the aerosol size distribution, refractive index, single-scattering albedo, and effect of nonsphericity on the phase function; the models are derived from analysis of ground-based remote sensing of the ambient column aerosol size distribution and in situ measurements; (5) inversion of the measured radiance at satellite level into the aerosol optical thickness, volume (or mass) concentration, and spectral radiative forcing using radiative transfer

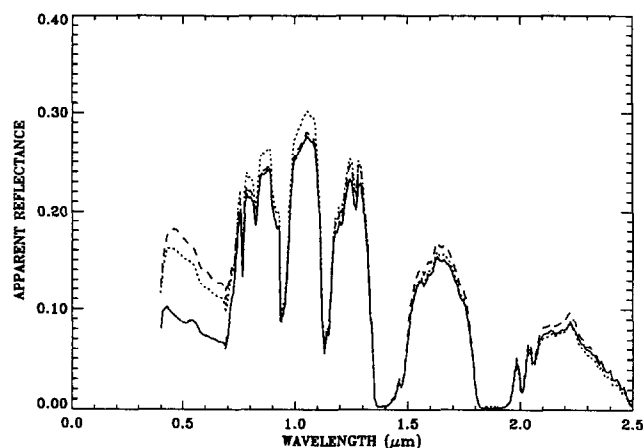


Figure 2. Spectral radiance measured from the airborne visible and infrared imaging spectrometer (AVIRIS) aircraft spectral imager over dry grassland in Stockton, northern California, acquired August 20, 1992, and plotted in the units of reflectance [Gao *et al.*, 1993]. The solid line is for the spectral surface reflectance in the presence of a clean atmosphere, while the dashed and dotted lines are for observations of a nearby surface through thin smoke originated from a wildfire (more smoke for the dashed line spectrum). The smoke has a large effect in the visible part of the spectrum, decreasing with wavelength from the blue to the red region. The effect is smaller than variation in the surface high reflectance in the near IR and is also negligible in the mid-IR ($2.2 \mu\text{m}$) due to the large ratio of the wavelength of radiation to the size of particles.

lookup tables computed for the dynamical aerosol models [e.g., Fraser *et al.*, 1992]. In the following we describe this approach and its physical bases.

Use of Dark Targets

The first application of dark targets for aerosol retrieval was based on detection of green forests as the dark pixels using the normalized difference vegetation index (NDVI) and the near-IR reflectance (KS88). Dark vegetation was determined by high NDVI and low reflectance in the near IR. For these pixels the surface reflectance in the red channel is assumed as $\rho = 0.02 \pm 0.01$ and used to derive the aerosol optical thickness. Application of the technique to Landsat multispectral scanner (MSS) data over the mid-Atlantic region of the United States showed a very good agreement against Sun photometer measurements (KS88). To derive the optical thickness from the path radiance, the aerosol size distribution, single-scattering albedo, and refractive index have to be assumed. Spherical and homogeneous particles need also to be assumed in order to use the Mie theory in the calculation, unless nonsphericity is identified [Kahn *et al.*, this issue] and modeled [Mishchenko and Travis, 1994; Nakajima *et al.*, 1989]. Sensitivity studies showed that in a general case, these assumptions can generate substantial errors in the derived aerosol optical thickness ($\sim 30\%$). To reduce the errors, a good model of aerosol properties based on measurements is required. In some regions where the model is most applicable, we can expect the remote sensing procedure to be more accurate. This was the case in the application of the method of KS88 to the mid-Atlantic region where the aerosol model was better known. KS88 applied the derived aerosol optical thickness for atmospheric corrections of remote sensing of the surface reflectance

and noticed that since the same assumptions are used in the derivation of the optical thickness from the path radiance and in the process of atmospheric correction, a large part of the errors in the aerosol model canceled out. This reduction in errors may occur also in the determination of the aerosol direct radiative forcing, which is closely linked to the path radiance used to derive the optical thickness. These topics are discussed later in the paper.

The determination of dark pixels using the vegetation index is not well suited for global applications since the vegetation index itself is affected by the aerosol, a feedback circle that causes the method to be applied only to images for which it is known a priori that dense vegetation pixels are present in the image. An alternative technique is suggested to locate the dark pixels using longer wavelengths (2.1 or $3.7 \mu\text{m}$) that are less sensitive to aerosol scattering (since their wavelength is much longer than the size of most aerosol particles) but still sensitive enough to the surface characteristics. Such wavelengths have been successfully used to find pixels that are dark in the visible channels [Holben *et al.*, 1992; Kaufman and Remer, 1994; Kaufman *et al.*, 1997].

Figure 2 demonstrates the spectral properties of vegetation and the effect of smoke aerosol as a function of wavelength. In this figure, spectral radiances from the AVIRIS aircraft spectral imager over dry grassland in California are plotted. The solid line is for the spectral surface reflectance in the presence of a clean atmosphere. The dashed and dotted lines are for observations of a nearby surface through thin smoke from a smoldering section of a wildfire, with more smoke in the dashed line spectrum. Smoke has a large effect in the visible part of the spectrum, decreasing in magnitude with wavelength from the blue to the red region. In the near-IR the effect is smaller than the variations in the surface reflectance between the smoke free area and the area affected by smoke. The smoke effect is not observable in the mid-IR ($2.2 \mu\text{m}$) due to the large ratio of the wavelength of radiation to the size of particles.

Analysis of advanced very high resolution radiometer (AVHRR) images over eastern United States and over Brazil shows that the AVHRR $3.7 \mu\text{m}$ channel, similar to the MODIS $3.8 \mu\text{m}$ channel, is not sensitive to the presence of pollution aerosol or smoke [Kaufman *et al.*, 1990b; Kaufman and Remer, 1994] but is very sensitive to the presence of forest pixels and can be used for their determination. The apparent reflectance in the $3.7 \mu\text{m}$ AVHRR channel is well correlated with the reflectance at $0.64 \mu\text{m}$ (see Figure 3), though the ratios between the surface reflectance at $3.7 \mu\text{m}$ and $0.64 \mu\text{m}$ change from day to day. Note that in order to use the reflective part of the $3.7 \mu\text{m}$ channel it has to be corrected for thermal emission and for absorption by water vapor [Roger and Vermote, 1997]. The variation in the relationships from day to day in Figure 3 may result from inaccuracy of the correction for emission and water vapor absorption. Nevertheless, several successful applications of this channel for remote sensing of smoke aerosol were reported [Holben *et al.*, 1992; Vermote *et al.*, this issue]. The application to MODIS should be significantly improved because of better instrument characterization and the availability of total precipitable water vapor information.

Figure 4 shows examples of the relationships between the surface reflectance at $2.1 \mu\text{m}$ and that at $0.47 \mu\text{m}$ and $0.64 \mu\text{m}$ derived from Landsat thematic mapper (TM) and airborne visible and infrared imaging spectrometer (AVIRIS) images over the mid-Atlantic United States. The reflectances were

corrected for the atmospheric effects based on ground-based measurements of the aerosol optical thickness. The images analyzed included forested area and crop land, as well as exposed soil, residential area, and water. The data were averaged for the specific surface types shown in Figure 5. The uncertainty in the estimate of surface reflectance in the visible channels from the $2.1 \mu\text{m}$ channel reflectance is ± 0.005 to ± 0.01 in the red and blue channels, respectively, for dark targets with reflectance at $2.1 \mu\text{m} < 0.10$. The measurements conducted in drier regions, San Diego, California, and in Brazil also show similar relationships between the reflectance in the blue, red, and $2.1 \mu\text{m}$ channels, but with the blue and red reflectances lowered by 10–20% from the predicted values as using the ratios in Figure 5. This issue is currently under intensive study to find how it can be applied globally and in which conditions it may fail (e.g., snow or water).

Since a MODIS nearby channel of $3.8 \mu\text{m}$, located around $4.0 \mu\text{m}$, is not sensitive to water vapor absorption, it prompted us to test if this channel is better for this application. Comparisons between the 3.8 and the $4.0 \mu\text{m}$ channels include results from errors due to atmospheric absorption and emission and errors due to uncertainty in the surface emissivity. The $4.0 \mu\text{m}$ channel is sensitive to N_2 absorption, which is about as strong as the water absorption at the MODIS $3.8 \mu\text{m}$ channel for a standard atmospheric model (vertical transmission of 90% due to H_2O at $3.8 \mu\text{m}$ and 88% due to N_2 at $4.0 \mu\text{m}$). Although N_2 absorption does not vary substantially and is well known, its emission, however, depends more on the temperature profile, in regard to the retrieval of surface reflectance. On the other hand, the $3.8 \mu\text{m}$ channel is more affected by the water vapor absorption. Sensitivity study shows that the effect of uncertainty in the vertical temperature profile on the error in the derived surface reflectance at $4.0 \mu\text{m}$ is only about 10%, while

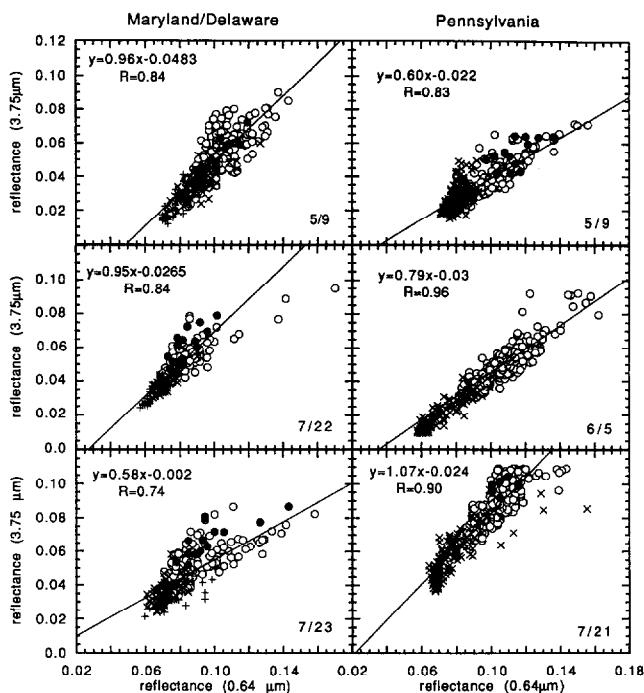


Figure 3. Scatter diagrams of the relationship between the apparent surface reflectance in the red ($0.64 \mu\text{m}$) and the mid-IR ($3.7 \mu\text{m}$) advanced very high resolution radiometer (AVHRR) channels (after Kaufman and Remer [1994] ©1994 IEEE).

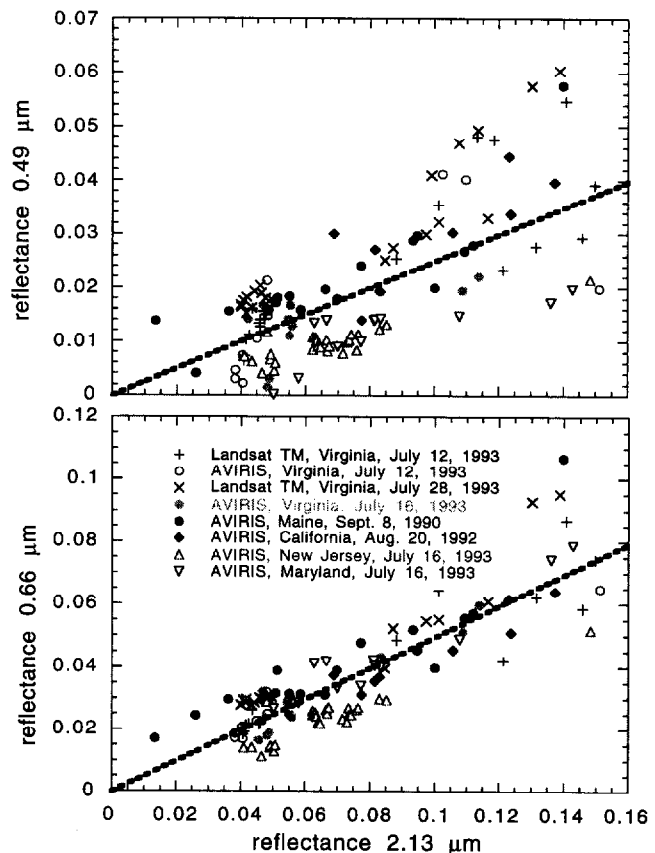


Figure 4. Scatter diagrams between the surface reflectance at $0.49 \mu\text{m}$ ($\rho_{0.49}$), $0.66 \mu\text{m}$ ($\rho_{0.66}$), and that at $2.2 \mu\text{m}$ ($\rho_{2.2}$). Different symbols are used for each of the Landsat thematic mapper (TM) or AVIRIS images (see notations in the bottom figure). The remotely sensed data were corrected for the atmospheric effect before display. The average relationships $\rho_{0.49}/\rho_{2.2} = 0.25$ and $\rho_{0.66}/\rho_{2.2} = 0.5$ are also plotted [Kaufman et al., 1997].

the effect of a 10% uncertainty in total precipitable water vapor on the $3.8 \mu\text{m}$ channel causes an error in the surface reflectance of 20%. So, in this account, the $4.0 \mu\text{m}$ channel is better than the $3.8 \mu\text{m}$ channel.

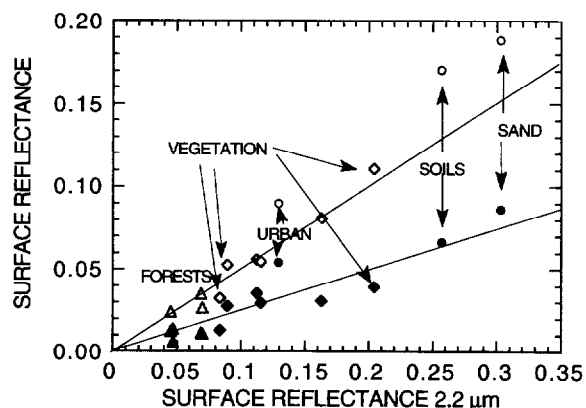


Figure 5. Scatter diagram between the surface reflectance at $0.49 \mu\text{m}$ (solid symbols) and $0.66 \mu\text{m}$ (open symbols) to that at $2.2 \mu\text{m}$ for several surface types. The average relationships $\rho_{0.49}/\rho_{2.2} = 0.25$ and $\rho_{0.66}/\rho_{2.2} = 0.5$ are also plotted (solid lines) [Kaufman et al., 1997].

However, because of the longer wavelength and the reduced solar brightness, the fraction of reflected sunlight at 4.0 μm is only 60% of that at 3.8 μm for the same surface reflectance. Since the reflectance at 3.8 or 4.0 μm is computed after correction for the emission by the atmosphere and surface using the 11 μm channel, the lower fraction of reflected light will double the errors associated to uncertainty in the surface emissivity at 11 μm . The uncertainty in emissivity at 11 μm of $\Delta\epsilon \pm 0.02$, as found, generates a 25% error in the surface reflectance at 3.8 μm (for $\rho_{3.8} = 0.025$) [Kaufman and Remer, 1994] and up to twice as large errors at 4.0 μm due to the smaller fraction of the reflected sunlight. This source of error is larger than the error due to uncertainty in atmospheric absorption. It therefore can be concluded that the 3.8 μm channel is better for the application of aerosol remote sensing.

Global Remote Sensing of Aerosol

The following procedure for global remote sensing of aerosol is emerging for the multispectral EOS-MODIS radiometer. The MODIS channels that are used in the analysis are the 250 m resolution 0.66 μm channel, the 500 m resolution 0.47 μm and 2.1 μm channels, and the 1 km resolution 3.8 and 11 μm channels. The 11 μm window channel is used to correct the 3.8 μm channel for emission from the surface. In addition, water vapor absorption channels around 0.94 μm and the 9.6 μm ozone channel are adopted for the correction of total precipitable water vapor and ozone absorption. Stratospheric aerosol effect will be estimated by using the MODIS 1.37 μm channel [Gao and Kaufman, 1995]. Cloud mask (or snow mask) is important in determining the cloud and snow (or ice) free pixels, which need also to be included. The automatic procedure to derive global distribution of aerosol optical thickness, mass concentration, and radiative forcing in cloud (or snow, ice) free regions is as follows:

Step 1

Selection of dark pixels and determination of their surface reflectance. The selection of the pixels in the MODIS image which are used to derive the aerosol optical thickness follows our experience with the 3.8 μm and 2.1 μm reflectances and their relationship to reflectance in the visible channels. The technique prioritizes the criteria in order to minimize the residual error in the predicted surface reflectance and, consequently, in the derived optical thickness. It may be biased by the broader experience with application of the 3.8 μm channel than the 2.1 μm channel for predicting the surface reflectance in the red channel and for remote sensing of aerosol [Holben *et al.*, 1992; Kaufman and Remer, 1994; Vermote *et al.*, this issue; Kaufman and Tanré, 1996; Kaufman *et al.*, 1997; Y. J. Kaufman and R. S. Fraser, manuscript in preparation, 1997]. We found that the highest accuracy in predicting the surface reflectance in the red and blue channels is for pixels that do not represent water and have a very low reflectance at 2.1 μm . When reflectance is larger than 0.05, the uncertainty in the relationship between the reflectance at 2.1 and 0.66 or 0.47 μm makes the 3.8 μm channel more attractive, despite the need to correct for surface emission. If the surface is not dark enough both at 2.1 and at 3.8 μm , the derivation of aerosol is still possible, but with lower expected accuracy due to higher (surface) reflectance at 2.1 μm [Kaufman *et al.*, 1997].

For a grid box of 10×10 pixels of 1 km resolution at nadir, and correspondingly higher number of 500 and 250 m pixels,

the number of the dark pixels $N_{\lambda i}$ that have an apparent mid-IR reflectance $\rho_{\lambda i}^*$ less than a threshold $\rho_{\lambda i}^{\text{th}}$ is determined on the basis of the following priority of criteria (the surface reflectance ρ_{λ}^s is indicated for each case):

Priority 1

$$N_{2.1a} \text{ for } 0.01 \leq \rho_{2.1}^* \leq 0.05 \quad (\rho_{0.47}^s = \rho_{2.1}^*/4, \rho_{0.66}^s = \rho_{2.1}^*/2)$$

Priority 2

$$N_{3.8} \text{ for } \rho_{3.8}^* \leq 0.025 \quad (\rho_{0.47}^s = 0.01, \rho_{0.66}^s = 0.02)$$

Priority 3

$$N_{2.1b} \text{ for } 0.01 \leq \rho_{2.1}^* \leq 0.10 \quad (\rho_{0.47}^s = \rho_{2.1}^*/4, \rho_{0.66}^s = \rho_{2.1}^*/2)$$

Priority 4

$$N_{2.1c} \text{ for } 0.01 \leq \rho_{2.1}^* \leq 0.15 \quad (\rho_{0.47}^s = \rho_{2.1}^*/4, \rho_{0.66}^s = \rho_{2.1}^*/2)$$

The criteria are used only over land surfaces excluding water, clouds, ice, and snow. The first criterion in this list that represents more than 5% of the pixels in the grid box is chosen to derive the optical thickness, though the results of lower priorities are also stored. The quality of the derivation is expected to decrease with the priority rank. The thresholds and surface reflectances determined are based on Figures 3–5. We do not use pixels with reflectance at 2.1 μm , $\rho_{2.1}^*$, larger than 0.15, since the relationship between the reflectance in the visible channels and the 2.1 μm channel is significantly more chaotic for $\rho_{2.1}^* > 0.15$ in some regions [Kaufman *et al.*, 1997]. The division into three segments of $\rho_{2.1}^*$ is based on the assumption (which is based on measurements of surface properties) that there is a higher probability for a larger absolute error obtained from a larger value of the surface reflectance. It is not clear how the 3.8 μm threshold relates to the 2.1 μm low threshold, since we did not yet have simultaneous remote sensing data in both channels to compare between them. We chose the 2.1 μm channel threshold as the first priority, because of the dependence of the 3.8 μm criterion on correction for the emissive part, in the presence of water vapor absorption.

Step 2

Preliminary derivation of the optical thickness. In the first stage, it is not clear which aerosol model should be used. Therefore the optical thickness is first derived in the red and blue channels from $\rho_{\lambda i}^*$ and $\rho_{\lambda i}^s$ using a continental aerosol model [Lenoble and Brogniez, 1984]. The parameters are given in Table 1. The derived optical thickness is expected to be affected from inaccuracies due to possible wrong choice of the scattering phase function and single-scattering albedo. The optical thickness is derived using a lookup table that relates a Lambertian surface reflectance to the measured radiance as a function of the optical thickness and the viewing and illumination geometry [e.g., Fraser *et al.*, 1984, 1992; Kaufman *et al.*, 1990]. The values of $\rho_{\lambda i}^*$ and $\rho_{\lambda i}^s$ used in retrieval of aerosol optical thickness are based on the average of 10–40 lowest percentile of the selected dark pixels within 10×10 km (at nadir), from which the standard deviation is also calculated.

Step 3

Determination of the aerosol model. The aerosol model is determined using the value of the optical thickness from step 2 and the ratio of the aerosol single-scattering path radiance $L_{p\lambda}$ ($L_{p\lambda} = \tau_{\lambda} P_{\lambda} \omega_{\lambda}$) in the red and blue channels. The

Table 1. Summary of Aerosol Dynamic Models

	r_g (μm)	r_v (μm)	σ	V_0 ($10^6 \text{ cm}^3/\text{cm}^2$)	ω_0 (670 nm)
<i>Continental Aerosol</i>					
Water soluble*	0.005	0.176	1.090	3.050	0.96
Dust-like	0.500	17.60	1.090	7.364	0.69
Soot	0.0118	0.050	0.693	0.105	0.16
<i>Biomass Burning</i>					
Accumulation	0.061	0.130	0.500	$-2.4 + 45\tau$	0.90†
Coarse	1.0–1.3 τ	6.0–11.3 $\tau + 61\tau^2$	0.69 + 0.81 τ	$2.4 - 6.3\tau + 37\tau^2$	0.84†
<i>Industrial/Urban Aerosol</i>					
Accumulation 1	0.036	0.106	0.60	$-2.0 + 70\tau - 196\tau^2 + 150\tau^3$	0.96
Accumulation 2	0.114	0.210	0.45	$0.34 - 7.6\tau + 80\tau^2 - 63\tau^3$	0.97
Salt	0.990	1.300	0.30	$-0.16 + 4.12\tau$	0.92
Coarse	0.670	9.500	0.94	1.92	0.88
<i>Dust Aerosol</i>					
Dust background					
mode 1	0.0010	0.0055	0.755	6.0×10^{-6}	0.015
mode 2	0.0218	1.230	1.160	1.0	0.95
mode 3	6.2400	21.50	0.638	0.6	0.62

Aerosol parameters of the continental model are from *Lenoble and Brogniez* [1984] and for the dust model from *Shettle* [1984]. Parameters of the aerosol models of industrial/urban and smoke used in the remote sensing procedure are after *Remer et al.* [1996, this issue], where the parameters are for a combination of lognormal size distributions given by the number distribution, or by the volume distribution:

$$\frac{dN}{d \ln r} = \frac{N_0}{\sigma \sqrt{2\pi}} \exp \left[-\frac{[\ln(r/r_g)]^2}{2\sigma^2} \right], \quad \frac{dV}{d \ln r} = V_0 \exp \left[-\frac{[\ln(r/r_v)]^2}{2\sigma^2} \right]$$

where N_0 is the number of particles per cross section of atmospheric column (cm^{-2}), r_g is the mean radius of the number distribution, σ is the standard deviation of $\ln(r)$, and r_v is the volume mean radius, $r_v = r_g \exp[3\sigma^2]$, V_0 is the column volume of the particles per cross section of atmospheric column (cm^3/cm^2), which is given by

$$V_0 = \frac{1}{\sigma \sqrt{2\pi}} e^{-9/2\sigma^2} N_0 \left(\frac{4\pi}{3} \right) r_v^3$$

The equation for r_g , r_v , σ , and V_0 should be applied for $\tau \leq 0.6$; for $\tau > 0.6$, the value $\tau = 0.6$ should be used.

*Water soluble aerosol of continental model is a wide mode encompassing both nuclei and accumulation modes.

†For biomass burning aerosol we use the same real and imaginary part of refractive index (i.e., $1.43 - 0.0035i$) as industrial aerosol but allow for external mixing of graphitic carbon. This results in greater absorption and smaller ω_0 . For the dust model, an aerosol of 2 km scale height was assumed to match the unit of V_0 .

derivation of the aerosol single-scattering path radiance from the total measured radiance is performed by using the same continental aerosol model as used to determine the aerosol optical thickness. This apparently contradicting application is based on the assumption that multiple scattering does not vary significantly with the aerosol model due to a lower sensitivity to the shape of the phase function. For small optical thicknesses $\tau_{\text{red}} < 0.15$, since the surface may introduce larger errors, we do not expect to derive the spectral aerosol radiance with a sufficient accuracy to determine the aerosol model. Therefore if $\tau_{\text{red}} < 0.15$, then the continental model is retained. Otherwise, if $L_{p\text{-red}}/L_{p\text{-blue}} > T_{h1}(\Theta)$, then the dust model should be used; if $L_{p\text{-red}}/L_{p\text{-blue}} < T_{h2}(\Theta)$, then the nondust model (i.e., smoke or urban/industrial aerosol model) is selected on the basis of the geographic locations and seasons as described below. Between the two thresholds $T_{h1}(\Theta)$ and $T_{h2}(\Theta)$, an interpolation of the models is applied. Such interpolation will result in a model that includes accumulation mode due to smoke or industrial/urban pollution and a coarse mode from soil dust, which in essence is a type of continental model. The values of the threshold as a function of the scattering angle Θ are based on theoretical computations of the ratio between the two path radiances (see Figure 6), which are given by the following: (1) for $40^\circ \leq \Theta \leq 150^\circ$, $T_{h1}(\Theta) = 0.90$ and $T_{h2}(\Theta) = 0.72$; (2) for $150^\circ \leq \Theta < 168^\circ$, $T_{h1}(\Theta) = 0.9 - 0.01(\Theta - 150)$ and $T_{h2}(\Theta) = 0.72$; (3) for $168^\circ \leq \Theta$, it is not

possible to distinguish between the aerosol types, and the phase function is not well predictable because of its strong dependence on size and shape of the particles.

For the nondust, noncontinental model cases the separation between zones with smoke aerosol and industrial/urban aerosol are performed on the basis of geographic locations and seasons (see Figure 7) [*d'Almeida et al.*, 1991; *Hao and Liu*, 1994; *Husar et al.*, this issue], which can be categorized in latitude and longitude zones as follows:

Industrial/urban aerosol

North America/Europe: (100°W–50°E; 30°N–70°N)

Southeast Asia: (105°E–150°E; 15°N–45°N)

Central America/Africa (May–Nov): (100°W–50°E; equator–30°N)

South America/Africa (Dec–April): (100°W–50°E; 65°S–equator)

Smoke

Central America/Africa (Dec–April): (100°W–50°E; equator–30°N)

South America/Africa (May–Nov): (100°W–50°E; 65°S–equator)
the rest of the world

It should be noted that this definition of zones of industrial/urban aerosol and smoke is experimental and preliminary. To be implemented into retrieval scheme, the cut into square boxes of latitude and longitude is necessary. However, it may

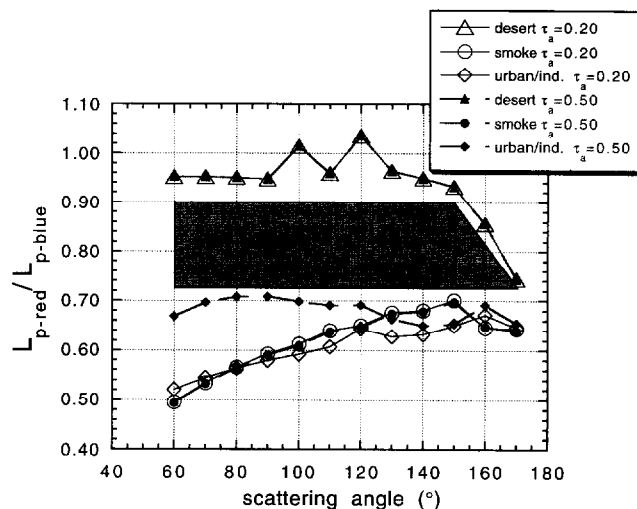


Figure 6. Ratio of the aerosol single-scattering path radiance L_p in the red and blue channels as a function of the scattering angle. The ratio is plotted for the dust, smoke, and urban/industrial model for two aerosol optical thicknesses. For dust background model, *Shettle* [1984] was used. For smoke from biomass burning and the urban/industrial aerosol the dynamic models [Remer et al., 1996] were used. The difference between the ratio for dust and nondust aerosol is used to distinguish between them. The gray zone is the separation zone between the dust and nondust algorithms.

show some types of aerosols that do not exist locally; for example, the dominant industrial/urban aerosol in Saudi Arabia and some parts of East Africa. Because of the bright desert surface, our algorithm cannot retrieve aerosol properties over those regions anyway with the present (automatic) procedures. For industrial/urban aerosol in Southeast Asia, in particular, more absorption is appropriate. Therefore $\omega_0 \approx 0.91$ should be used as compared with $\omega_0 \approx 0.97$ in North America and Europe [Liou et al., 1996]. The Antarctic continent ($>65^\circ\text{S}$) and the Arctic region ($>70^\circ\text{N}$) are not considered in this study. To be more confident of the regions for different types of aerosols, it is currently being evaluated by using the Sulfate Cloud and Radiation (SCAR) database (see the aerosol model section) and any possible related information and will be certainly reevaluated globally after the MODIS launch.

Step 4

Reconfiguration of the optical thickness. When the aerosol model is determined, the optical thicknesses τ_{red} and τ_{blue} can be corrected for the difference between the newly determined aerosol model and the previously used continental model. Present correction is based on the aerosol single-scattering radiance $L_{p\lambda}$ derived from the MODIS measured radiance. This radiance (see equation (2)), expressed by aerosol parameters from the continental model, is

$$L_{p\lambda} = \tau_{\lambda}^{\text{cont}} P_{\lambda}^{\text{cont}} \omega_{\lambda}^{\text{cont}} / (4\mu \mu_0) \quad (3)$$

The same single-scattering path radiance can be now expressed by the parameters from the new model, which is

$$L_{p\lambda} = \tau_{\lambda}^{\text{new}} P_{\lambda}^{\text{new}} \omega_{\lambda}^{\text{new}} / (4\mu \mu_0) \quad (4)$$

As a result, the aerosol optical thickness for the new model $\tau_{\lambda}^{\text{new}}$ can be derived as follows:

$$\tau_{\lambda}^{\text{new}} = \tau_{\lambda}^{\text{cont}} \frac{P_{\lambda}^{\text{cont}} \omega_{\lambda}^{\text{cont}}}{P_{\lambda}^{\text{new}} \omega_{\lambda}^{\text{new}}} \quad (5)$$

As in step 3, the assumption behind this transformation is also that the differences between the phase functions and the single-scattering albedos do not affect the multiple scattering, but they do affect the single-scattering radiance. For high optical thickness, where multiple scattering is more important, we may expect errors in the single-scattering albedo to be more significant. Then new full radiative transfer lookup tables for the specific models will be used. The “new” values of P_{new} and ω_{new} are derived from the dynamic models as discussed in the next section and given in Table 1.

Step 5

Subgrid calculations. In some specific cases, for example, close to sources of smoke aerosol, the resolution of 10×10 km at nadir may be too crude to capture the strong spatial variability. If these sources are located in a region with the surface densely covered by dark targets, then a finer resolution is justified and possible. In the previous steps, the aerosol optical thickness τ_{λ} and standard deviation σ_{λ} were derived in the red and blue channels for the nominal resolution of 10×10 km at nadir. If the ratio of $\sigma_{\lambda}/\tau_{\lambda} > 0.5$, then the variability of the aerosol is significant. If the number of dark targets, in the 500 m resolution, used in the analysis, N , is >30 , then the grid box is separated into four smaller boxes of 5×5 pixels, and the analysis is redone for the average of 10–60 percentile, instead of 10–40. The averaged optical thicknesses in the two channels from each subbox are stored as an additional information in the data stream for the 10×10 km grid.

Aerosol Model

At a global scale, aerosol climatology was summarized by *d’Almeida et al.* [1991] as an expansion of the work of *Shettle*

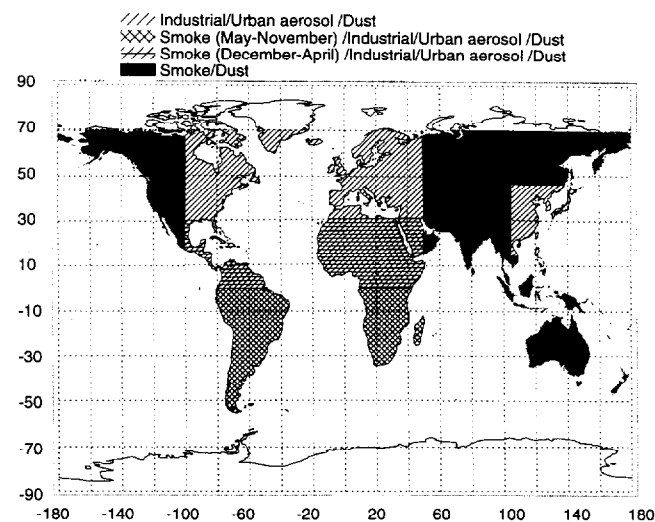


Figure 7. Map of the global distribution of assumed regions of smoke and urban/industrial aerosols based on *d’Almeida et al.* [1991], *Hao and Liu* [1994], and *Husar et al.* [this issue]. Note that in this figure we do not attempt to separate dust from smoke or industrial/urban aerosol in the algorithm based upon the spectral dependence of the path radiance.

and Fenn [1979]. They showed a compilation of a large amount of data and tabulated the dominant types of tropospheric aerosols as a function of the latitude, longitude, and the season. From the physical aerosol properties of refractive index and size distributions, they also computed the optical properties at the same spatial and temporal scales for extinction coefficient, single-scattering albedo, asymmetry factor, and phase function. Other studies were devoted to specific aerosols types: desert aerosols [d'Almeida, 1987; Shettle, 1984], maritime aerosols [Hoppel et al., 1990], or aerosols resulting from biomass burning in tropical regions [Crutzen and Andreae, 1990; Kaufman et al., 1992]. Therefore the climatology established is based on the existing measurements, most of them taken at ground level. There is a danger that these measurements often do not represent the whole atmospheric column or the properties of the ambient aerosol. Hegg et al. [1995] showed recently, using the data derived from the Sulfate Cloud and Radiation experiment-Atlantic (SCAR A), that the aerosol size distribution varies with altitude in the Northeast United States. Optical measurements from ground-based Sun/sky radiometers [Kaufman et al., 1994; Holben et al., 1996] are used to supplement the climatology with ambient aerosol measurements integrated on the whole column [Kaufman and Holben, 1996; Remer et al., 1996]. These measurements are in good agreement with in situ measurements of the size distribution and the aerosol chemistry measured from aircraft [Hegg et al., 1995; Hobbs et al., 1996; Remer et al., this issue].

Spectral aerosol optical thickness can be obtained from Sun photometer measurements [Volz, 1954; Flowers et al., 1969; Petterson et al., 1981]. Several local Sun photometer networks were used to detect various types of aerosols. Flowers et al. [1969] carried on a network over the United States from 1961 to 1966; d'Almeida et al. [1983] performed a similar experiment over North and West Africa from 1980 to 1982 with 11 instruments; Holben et al. [1991] conducted a similar effort in the Sahel from 1984 to 1986 using 15 monitoring stations. An extension of the measurements to derive the aerosol size distribution and scattering phase function was performed by using inversion of solar almucantar measurements [Kaufman et al., 1994]. Single-scattering albedo can be estimated from the collection of particles on filters, preferably by aircraft sampling of the entire atmospheric boundary layer and from the measurements of their absorption [Radke et al., 1991], or alternatively determined from accurate measurements of the downward flux or radiance [King, 1979; Wang and Gordon, 1993].

A Sun photometer network, the Background Air Pollution Monitoring Network (BAPMON), operating on a global and daily scales by World Meteorological Organization, can be used for correcting satellite images. However, a report from Forgan et al. [1994] pointed out the shortcomings of BAPMON measurements for poor calibration of the instruments and the lack of monitoring of the data quality. The measurements with an improved Aerosol Robot Network (AERONET) of automatic Sun/sky radiometers conducted recently in the Amazon Basin during intense biomass burning [Holben et al., 1996]; in Africa during dust events and in the eastern United States in the presence of industrial and urban pollution [Kaufman and Holben, 1996] seems to be well suited to our needs. The instrument measures in addition to the solar direct flux (e.g., Sun photometry) also the sky and aureole radiance distribution. The information can be used to derive aerosol properties of the optical thickness, the size distribution from 0.10 to 5 μm , the aerosol total loading, and the scattering phase function

[King et al., 1978; Nakajima et al., 1986; Kaufman et al., 1994; Holben et al., 1996]. In order to maintain high data quality the instruments transmit the data through satellite communication networks (GOES and Meteosat) in real time to a center where the data are analyzed. Because of the easy maintenance and central network communication capability, there are plans to expand aerosol measurements using such networks, as part of the international research and monitoring activities and as part of the support and validation of analysis of remote sensing from future satellite systems (the Earth Observing System, EOS of NASA, and POLDER/ADEOS mission of Centre National d'Etudes Spatiales (France)/National Space Development Agency of Japan).

In the last 3 years, three AERONET deployments have been part of the SCAR series of field experiments. The SCAR A experiment was conducted in the mid-Atlantic region of the United States in July 1993, measuring aerosol dominated by industrial/urban pollution. The SCAR C experiment in September–October 1994 was conducted in the northwestern United States to measure emissions from prescribed and wild-fires in midlatitudes. The SCAR B experiment in August–September 1995 in Brazil was targeted to deforestation and cerrado fires in the tropics during the dry season, with some data already collected from 1993. The aerosol size distributions that result from the AERONET deployments are shown in Figure 8 for the smoke aerosol (top graph) and for aerosol resultant from industrial/urban pollution (bottom graph). The SCAR database includes remote sensing measurements by the MODIS airborne simulator (MAS) and the AVIRIS spectral imager operated from the ER-2 aircraft flying at 20 km altitude, as well as in situ aerosol measurements taken by the instrumented C-131A aircraft of the University of Washington [e.g., Hobbs et al., 1996; Martins et al., 1996], and AERONET measurements of optical thickness and skylight. These data will be used later in the validation.

For the industrial/urban aerosol the model is based on 160 sky measurements collected during the SCAR A experiment, inverted into the aerosol volume size distribution, corrected for inversion problems [Remer et al., this issue] and analyzed as a function of the optical thickness [Kaufman and Holben, 1996; Remer et al., 1996]. Similar analysis is performed for smoke from the cerrado region in Brazil in 1993. In general, four main modes of aerosol can be distinguished in this data set:

1. For particle radius $r < 0.3 \mu\text{m}$, the aerosol accumulation mode is composed of particles formed from condensation of hot organic gases from the fire or from oxidation of trace gases (e.g., sulfates, organic particles, nitrates) for the urban/industrial aerosol. The volume of this mode increases with the optical thickness. The average size of the particles is fixed for biomass burning but increase with optical thickness for the urban/industrial aerosol. In this case, the increase in optical thickness is associated with more stagnant conditions with older (bigger) particles and higher humidity (more liquid water in the particle). The stagnant conditions also allow more time for cloud interactions that increase the particle size [Hoppel et al., 1990; Kaufman and Tanré, 1994].

2. For particle radius $0.3 \mu\text{m} < r < 0.8 \mu\text{m}$, the troposphere has few particles, and for the lower range of optical thickness the stratospheric aerosol volume distribution is seen [see also Kaufman et al., 1994; Shiobara et al., 1991]. Note that the stratospheric mode is excluded in the calculation of single-scattering albedo, phase function, and in the retrieval of aero-

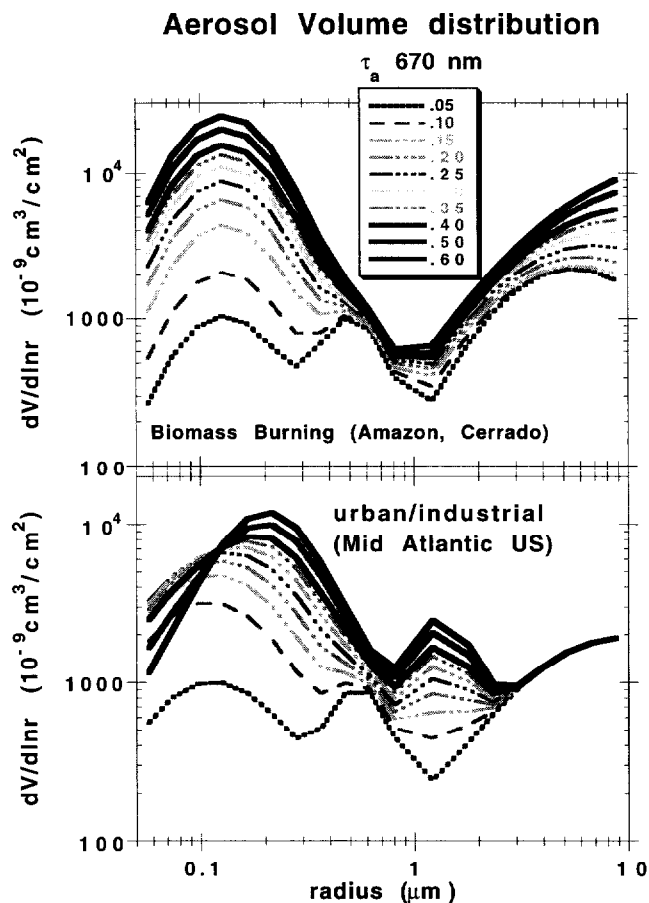


Figure 8. Aerosol models derived from Aerosol Robot Network (AERONET) 2 deployments, in the Amazon for the smoke aerosol (top graph) and in the mid-Atlantic region of the United States for an industrial/urban aerosol (bottom graph) in 1993 [after Remer et al., 1996]. Four main modes of aerosol can be distinguished: for particle radius $r < 0.3 \mu\text{m}$, accumulation mode of mostly organic smoke particles or sulfates in the urban/industrial aerosol; for $0.3 \mu\text{m} < r < 0.8 \mu\text{m}$, the troposphere has few particles and the stratospheric aerosol is observed; for $0.8 \mu\text{m} < r < 2.5 \mu\text{m}$, the maritime salt particle mode for the mid-Atlantic region only; for $2.5 \mu\text{m} < r$, the coarse particle mode.

sol properties in this paper. Instead, the correction for stratospheric aerosol is performed.

3. For particle radius $0.8 \mu\text{m} < r < 2.5 \mu\text{m}$, the maritime salt particle mode is derived in the mid-Atlantic region only, with volume that also increases with the total aerosol optical thickness. No salt particles are observed in the middle of South America for the smoke aerosol.

4. For particle radius $2.5 \mu\text{m} < r$, we have the coarse particle mode. For smoke aerosol these particles are also generated in the fire as ash or soil particles suspended in the air by the strong convection. Thus for smoke the coarse mode is correlated with the accumulation mode and the optical thickness. For the industrial/urban aerosol the coarse mode has an independent source with a short lifetime and is not correlated with other particle modes.

The model parameters are summarized in Table 1. They represent specific average conditions but include, in most cases, the average variation with the optical thickness. How-

ever, in some particular conditions the aerosol properties may still vary. For example, Sokolik and Toon [1996] cite several models of dust aerosol with single-scattering albedo varying between 0.6 and 0.95 for $\lambda = 0.45 \mu\text{m}$ and 0.7–0.95 for $\lambda = 1 \mu\text{m}$. Asymmetry parameter also varies in these models between 0.65 and 1.0. As they pointed out, it is not clear to what degree this variability is because of the difference between the measurements, or because of the difference in the dust properties. Though, for nondust conditions, measurements distributed around the world [Kaufman, 1993] show only a small variability of the path radiance for a given aerosol optical thickness ($\pm 20\%$). The single-scattering albedos of smoke and industrial/urban aerosol tabulated in Table 1 are default values. Currently, a study is being conducted to derive a global map of ω_0 using AERONET measurements and other in situ and remote measurements. The single-scattering phase functions shown in Figure 9 are derived with parameters tabulated in Table 1 for different aerosol models. The continental model has a phase function value that varies intermediately between the different models. The smaller smoke particles result in phase function that for the backscattering angles is a factor of 2 larger than the phase function for the urban/industrial aerosol. The dust phase function varies as a function of scattering angle from values similar to the urban/industrial aerosol for scattering angles of 100° – 130° to that of smoke around 160° and larger than both of them for scattering angles $> 160^\circ$, though smaller variability is expected in the presence of non-sphericity in the dust particles.

Uncertainty, Validation, and Quality Control

The main source of errors in the derived aerosol optical thickness is uncertainty in the surface reflectance and in the

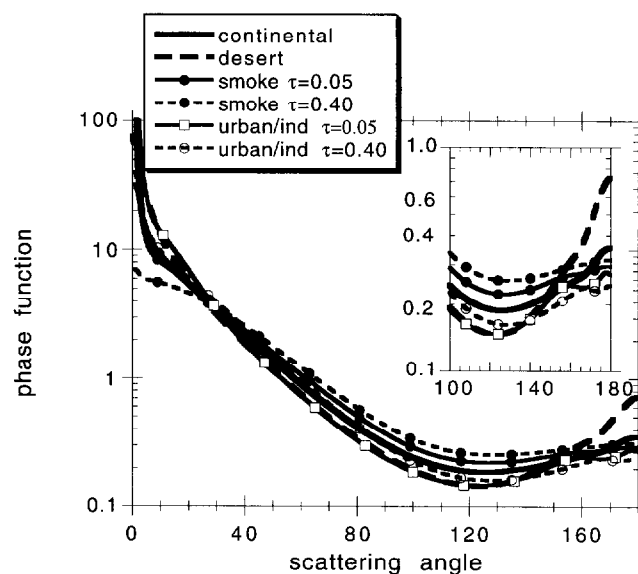


Figure 9. Scattering phase functions at $0.67 \mu\text{m}$ for four aerosol models: continental model [Lenoble and Brogniez, 1984]; desert dust model [Shettle, 1984]; smoke model from biomass burning [Kaufman and Holben, 1996; Remer et al., 1996]; urban/industrial aerosol model for measurements from Sulfate Cloud and Radiation (SCAR A) experiment [Remer et al., 1996]. The latest two models are given for two aerosol optical thicknesses but excluding the effects of stratospheric aerosol.

aerosol model. From theoretical considerations [Kaufman and Sendra, 1988] and empirical verifications [Fraser et al., 1984; King et al., 1992; Soufflet et al., 1997] the error is expected to be $\Delta\tau = \pm 0.05$ to ± 0.1 for small optical thickness and increasing to 20–30% for high optical thickness. These errors are based on knowledge of the uncertainty of surface reflectance within $\Delta\rho = \pm 0.005$ for the first two priorities in selecting dark targets (see step 1), and $\Delta\rho = \pm 0.01$ for the other two, and on a choice of the right aerosol model that describes the range of the aerosol effective radius and single-scattering albedo, to result in an error in the product $P\omega_0$ of $\pm 20\%$ in most cases. Despite the large effort to characterize the spectral properties of surface reflectance [Kaufman et al., 1997] and the large-scale validation efforts performed (see also discussion later on), there may be still unexpected problems. One such problem is small amounts of snow remaining on the ground. As found, 1% of the pixel covered by snow may cause an overestimate of the optical thickness by 0.1. We plan to reduce the effect of this particular problem by avoiding analysis of the data the first week after the snow melted. Other problems that we shall try to address before launch and which may remain as problems in some regions are the values of the aerosol single-scattering albedo and refractive index.

After the launch of MODIS on EOS, a continued validation and modification of the algorithms is planned by using continuous measurements from the AERONET ground network of Sun photometers/sky radiometers and in situ measurements. We expect to have over 60 instruments operational worldwide. They will be located in regions with key aerosol types or in regions where the aerosol type is expected to vary. This includes islands where ground-based in situ aerosol chemical, physical, and optical properties are measured [e.g., Prospero and Nees, 1986]. The MODIS-derived aerosol optical thickness and type will be compared with aerosol information measured in these stations. Consistency checks will be performed to observe the possible dependence of the optical thickness on the viewing direction. In addition, the results will be compared with optical thickness generated by other instruments, such as the MISR multiangle instrument also on EOS and the POLDER instrument on ADEOS launched successfully in August 1996 [Bréon et al., this issue]. Both POLDER, flown before MODIS, and MISR, flown simultaneously with MODIS, will be differently sensitive to the aerosol signals. POLDER will be sensitive to aerosol polarization, and both sensors will be sensitive to the aerosol angular optical properties. In particular, the MISR multiangle radiance measurements are planned to be used to estimate the aerosol nonsphericity [Kahn et al., this issue]. This information can be used to update the dust aerosol scattering phase function applied to specific geographic regions (e.g., Saharan dust, Gobi Desert dust) and used for time intervals for which the MODIS data are analyzed.

Application and validation of the remote sensing approach using the MODIS 2.1 μm channel to detect the dark pixels and determine their reflectance is shown in Figure 10 and Plate 1. In Figure 10 the aerosol optical thickness is derived from six Landsat TM and AVIRIS images collected during the SCAR A experiment and compared with aerosol optical thickness measured from the ground by the Sun photometer AERONET network. An example of a Landsat image and its analysis is shown in false color, representing the apparent reflectance of the Earth-atmosphere (top panels) and the derived optical thicknesses in the red and blue channels (bottom panels) in Plate 1. In the TM image, an elevated aerosol level accompa-

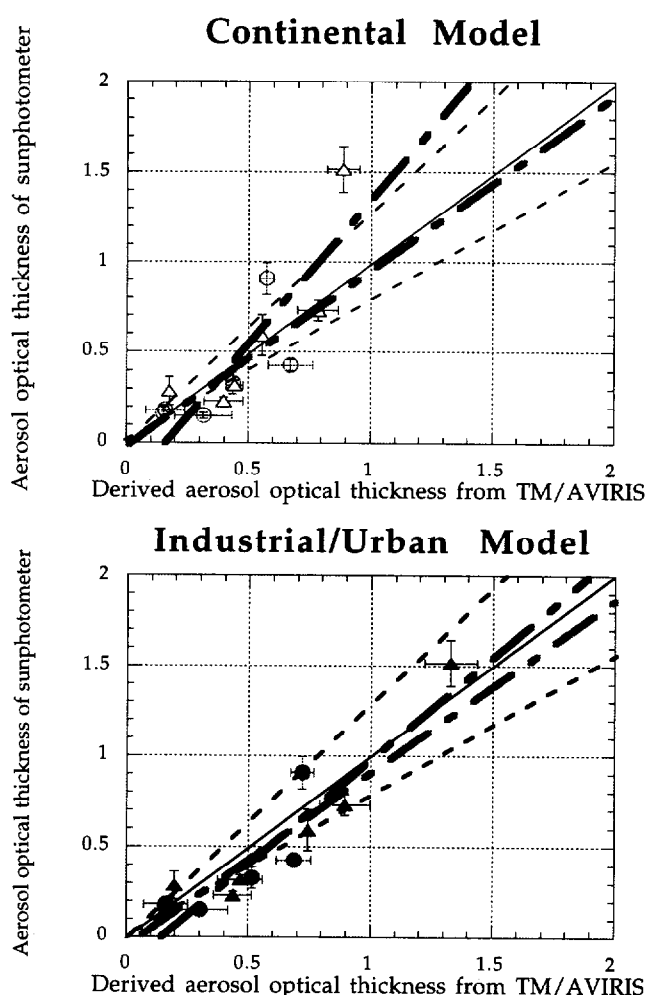


Figure 10. Comparison between aerosol optical thickness derived from Landsat TM and AVIRIS data collected during the SCAR A experiment and those from ground by AERONET Sun photometer. Circles are for red channel (i.e., 0.66 μm) and triangles are for blue channel (0.47 μm). Open symbols are for continental model and closed symbols are for industrial/urban model. The Landsat and AVIRIS data were averaged before analysis to the MODIS resolutions. Results of using a continental model and in the final analysis using appropriate dynamical model are shown. The standard deviations derived are the temporal variability of the Sun photometer data around the Landsat pass and the spatial variability of the optical thickness derived from the TM data around the location of the Sun photometer. The thin dashed lines are the range of the expected accuracy of $\pm 0.05 \pm 0.2\tau$ (with bias of ± 0.05 and an uncertainty in the slope of ± 0.2). Linear regression results are also provided (dotted-dashed lines).

nied by moisture and clouds is located in the top right and bottom part of the image. Excluding clouds, the corresponding higher optical thickness is derived. The images were averaged before analysis of the optical thickness to the MODIS resolution. It is an important step to simulate MODIS vision like observations. Both the results of analysis using the preliminary continental model and of the final analysis using the appropriate dynamical model are shown in Figure 10. In Plate 1, only the final corrected optical thickness is shown. The resolution of the aerosol optical thickness in Plate 1 is 10×10 km resolution that will be produced by MODIS operationally. One can see in

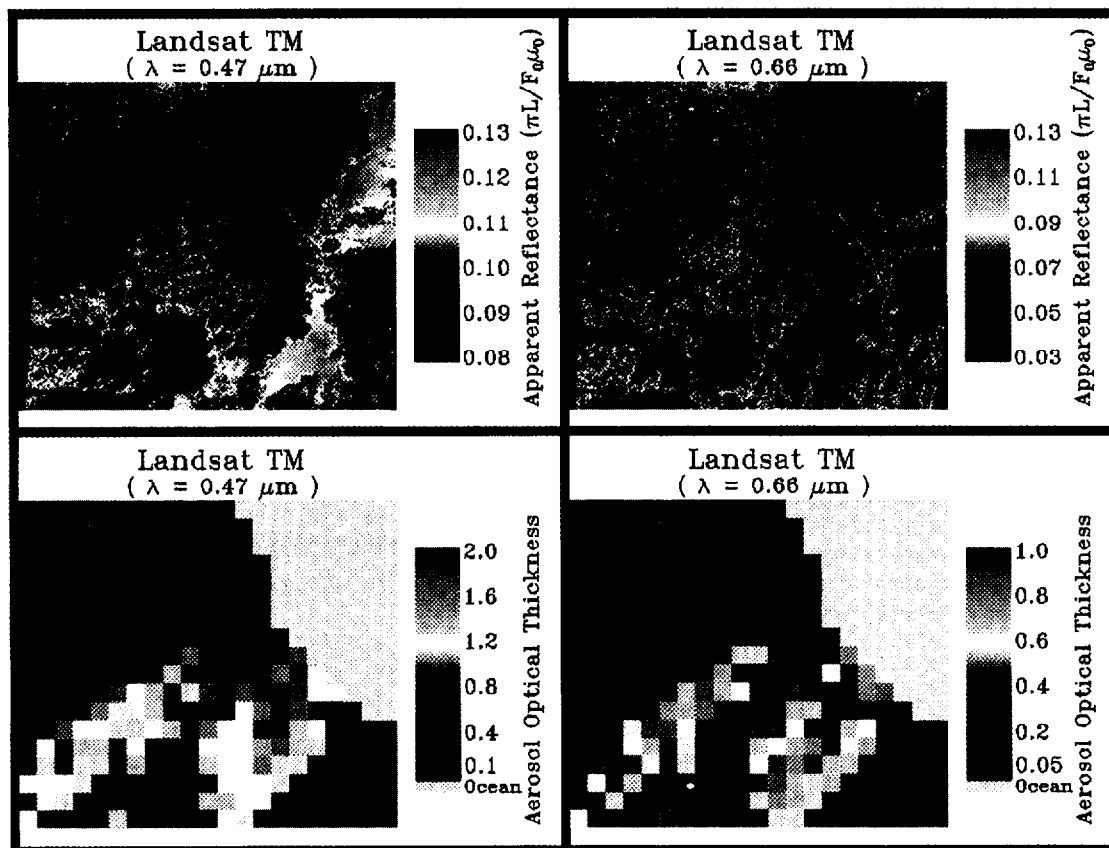


Plate 1. False color Landsat TM images over the North Carolina-Virginia region (July 12, 1993). The apparent reflectance of TM 0.47 μm channel (left) and 0.66 μm channel (right) are shown in the top panels. The bottom panels are the corresponding aerosol optical thickness derived of 10×10 km resolution using the MODIS algorithm for the reduced resolution Landsat images.

Figure 10 that the correction of the model is a significant improvement to the optical thickness, especially for high optical thickness. The standard deviations in Figure 10 are the temporal variability of the Sun photometer data around the Landsat overpass (abscissa) and the spatial variability of the optical thickness derived from the TM data around the locations of the Sun photometer (ordinate). The derived optical thickness using the dynamic aerosol models is within the expected range of uncertainties ($\Delta\tau_a = \pm 0.05 \pm 0.2\tau_a$). The improvement of the dynamic model is substantial. Note that the ratio between the surface reflectance in the red and blue channels and that in the mid-IR was derived mainly by using the data from SCAR A experiment. Also the dynamical aerosol model for industrial/urban aerosol was derived for SCAR A. Therefore the validation of Figure 10 was derived in the most favorable conditions. Comparison for independent cases is under way.

The combined land and ocean results of aerosol optical thickness at 0.55 μm is shown in Plate 2 (bottom panel) to accommodate the results derived from MODIS ocean algorithm [Tanré *et al.*, this issue]. Over land, since aerosol optical thickness at 0.55 μm is interpolated in logarithm scale from the values of red and blue channels (as shown in Plate 1), the apparent reflectance at 0.55 μm (top panel in Plate 2) is for reference only. Both results of land and ocean compare well.

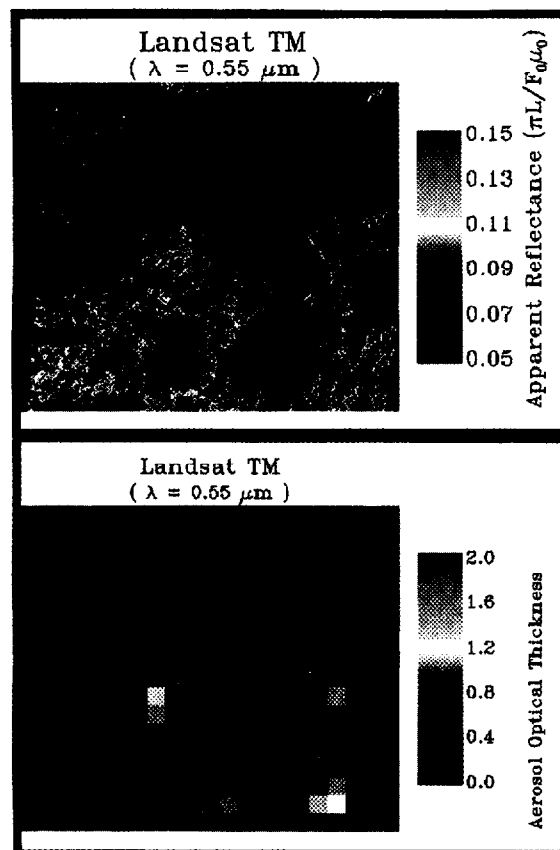


Plate 2. (opposite) Same as Plate 1 except for results at 0.55 μm and for both land and ocean combined.

The black pixels shown along the seashore are due to the deficiency of the ocean algorithm in coastal zones.

An application of the MODIS remote sensing technique to the South Atlantic region in Brazil and its validation is shown in Figure 6 of *Vermote et al.* [this issue]. They derived the aerosol optical thickness from the AVHRR data using dark targets identified with the $3.7\text{ }\mu\text{m}$ channel and a smoke aerosol model. The results compared against the AERONET measurements of the optical thickness (shown here in Figure 11) reveal a high correlation (with correlation coefficient equal to 0.93) between the remotely sensed values and the ground-based measurements. The uncertainty in the derivation is within the stated uncertainties of the procedure ($\pm 0.05 \pm 0.2\tau$), as displayed in the figure. Additional validation efforts are reported by *Vermote et al.* [this issue].

Columnar Aerosol Mass, Aerosol Surface Area and Radiative Forcing

The aerosol optical thickness describes the aerosol optical opacity for direct penetration of solar radiation. It is used in radiative transfer models to calculate the aerosol direct radiative forcing and for atmospheric corrections. It can also be inverted into the aerosol mass. The inversion of the measured radiance (or path radiance, after exclusion of surface reflectance) to the aerosol optical thickness, the columnar aerosol mass concentration (we refer here to mass for a unit specific weight of the aerosol), particle surface area (important for chemical processes), and the radiative forcing requires assumptions on the aerosol models and, in particular, the aerosol size distribution and refractive index. For large particles, it is also influenced by the particle nonsphericity. However, the errors associated with the derivations of the optical thickness from the detected radiance and the derivation of the aerosol mass and radiative forcing from the optical thickness are neg-

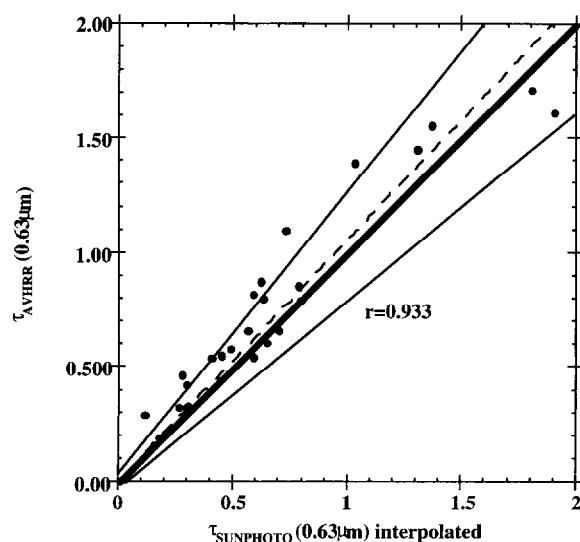


Figure 11. Comparison of retrieved optical thickness using AVHRR data and dark target approach with the measured optical depth from the AERONET Sun photometers over Brazil in 1993 [*Vermote et al.*, this issue]. The dashed line is the least squares fit to the results. The solid lines show the range of the expected accuracy of the algorithm. Most points are within the range of expected accuracy. Smoke aerosol model was used in the remote sensing procedure.

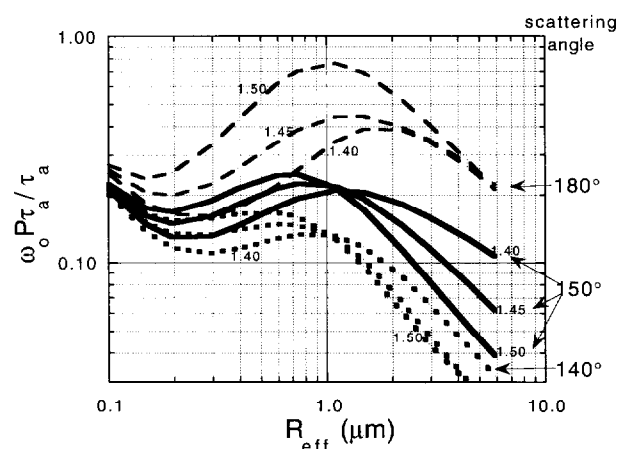


Figure 12. Effect of particle size on remote sensing of optical thickness. The ratio of the path radiance ($\omega_0 P \tau_a$) to the optical thickness (τ_a) are plotted as a function of the effective radius for three scattering angles (140° , 150° , and 180° indicated on the right-hand side of the figure) and three refractive indices (1.40, 1.45, and 1.50 indicated for most of the graphs). For a scattering angle of 150° the variation (values 0.13–0.24) with R_{eff} is minimal for effective radius from 0.1 to $1.5\text{ }\mu\text{m}$, though for 140° scattering angle, semilinear figure (values varying 0.11–0.16) in a narrower radius range $0.15\text{--}0.7\text{ }\mu\text{m}$ radius is obtained.

atively correlated. Therefore the total error in the final product (e.g., radiative forcing) is smaller than expected from the sum of the errors in each individual step. *Boucher and Anderson* [1995] developed this approach in the evaluation of the aerosol radiative forcing of climate. A similar approach is being developed for remote sensing of aerosols and their radiative forcing. The effect of uncertainty in the particle size on remote sensing may also depend on the scattering angle between the solar rays and the satellite observation [*Koepke and Quenzel*, 1979; *R. B. Husar*, private communication, 1995]. Therefore some scattering angles may be preferential for some applications. Figures 12–14 are used to explore these ideas. In these figures, the ratios of the aerosol single-scattering path radiance to the aerosol optical thickness (Figure 12), to the aerosol mass concentration and particle surface area (Figure 13), and to the aerosol radiative forcing for zero surface reflectance (Fig. 14) are plotted as a function of the aerosol effective radius of a lognormal distribution with a standard deviation (of the natural logarithm of the particle size) $\sigma = 0.6$. The calculations are for three refractive indices (1.40, 1.45, and 1.50 with an imaginary part of 0.0035) and selected scattering angles that represent the optimum choice of the scattering angle.

For remote sensing of the accumulation mode aerosol (effective radius between 0.1 and $0.5\text{ }\mu\text{m}$), the optimum derivation of the optical thickness is for scattering angles of 140° to 160° (depending on the possible range of the particle size), with an anticipated error due to uncertainty in the particle size and refractive index of ± 20 to $\pm 40\%$ (see Figure 12). Remote sensing of the columnar mass concentration is expected to be more accurate for the accumulation mode particles (effective radius $< 0.5\text{ }\mu\text{m}$) and is also best for a scattering angle of $120^\circ\text{--}150^\circ$ with uncertainty from particle size of ± 10 to $\pm 30\%$, and $\pm 30\%$ due to uncertainty in the refractive index (Figure 13 shows the results for a scattering angle of 150°). The particle surface area can be sensed for the coarse mode with an error

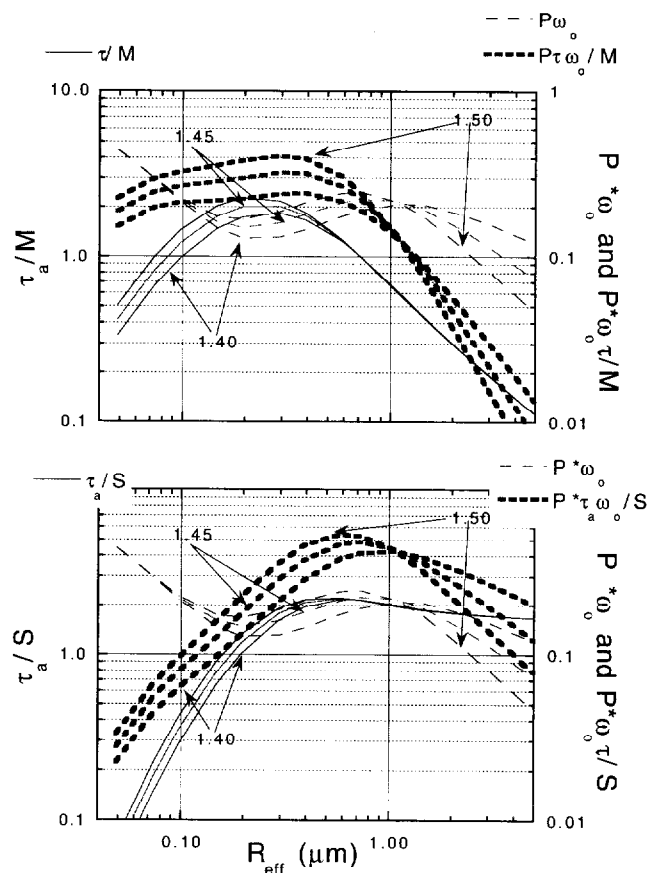


Figure 13. Effect of particle size on remote sensing of the aerosol mass. The aerosol mass sensitivity is given by the ratio of $L_{\text{path}}/M = P\omega_0\tau_a/M$. Results are shown for scattering angle of 150° only, the optimum angle for remote sensing of aerosol mass. Here, in the figures, this function as well as $P\omega_0$ and τ_a/M are plotted separately as a function of R_{eff} . The refractive index is also indicated. For refractive index equal to 1.40, the dependence on R_{eff} is found to be small between $R_{\text{eff}} = 0.1$ and $0.5 \mu\text{m}$. For larger refractive index the dependence is significantly larger. The ratios of L_{path}/M depend strongly on the refractive index. Therefore conversion of aerosol optical thickness to mass depends on reasonable knowledge of the refractive index.

of 30–50%, depending on the refractive index (about equal to the error in the optical thickness). The error introduced in remote sensing of the radiative forcing is only $\pm 20\%$ for a scattering angle of 140° for particle sizes between 0.1 and $1.0 \mu\text{m}$ radius (Figure 14). This higher accuracy in the direct forcing from MODIS, than the optical thickness, is an important finding. It is a result of the similar physics in the radiance measured from space above dark surfaces and the reflection by aerosol of the solar irradiance. Deriving the aerosol properties for a specific scattering angle will also result in a better precision, because of elimination of part of the variability in the uncertainty in the aerosol scattering phase function. The use of dynamic aerosol models, described before, is expected to reduce these errors further by limiting the effect of the uncertainty in the particle size. In order to use this error reduction associated with selecting specific viewing directions, we anticipate to group the aerosol products (optical thickness, mass concentration, and radiative forcing) for a resolution of 0.5° (in

equal angle and equal area) and for periods of time of 8 days and 1 month. This is in addition to a direct $10 \times 10 \text{ km}$ resolution (at nadir) daily aerosol product. Both arithmetic averages and scattering angle weighted averages are planned. Information on winds generated by the global circulation models that are based on radiosonde measurements will be also stored and averaged by the weightings of aerosol concentration in order to derive the aerosol fluxes [e.g., Fraser et al., 1984]. The spectral radiative forcing will be generated only for the reduced resolution. Because of large uncertainty in the single-scattering albedo ω_0 we plan to record the aerosol radiative forcing for zero surface reflectance only, for which the radiative forcing is completely contributed by aerosol.

For the orbital parameters from the EOS system and the scanning directions of MODIS, Figure 15 shows the coverage of the latitude zones for which a scattering angle of 150° can be derived as a function of the month. The scattering angles of 140° – 150° , as found, can be reached for the most important aerosol types, in the tropics for smoke all year-round and in summer months for urban/industrial aerosol in the northern hemisphere, up to a latitude of 40°N .

Conclusions

After the launch of MODIS sensors on the EOS satellites, daily or twice daily aerosol optical thickness will be operationally derived over the land (as well as over the ocean) and used to derive the aerosol columnar mass distribution and radiative forcing. Despite the difficulties to derive aerosol over the land, it is expected that using dark targets as identified by their reflectance in the mid-IR, the aerosol optical thickness τ_a can be sensed with an estimated error of $\Delta\tau_a = \pm 0.05 \pm 0.2\tau_a$ over the vegetated and partially vegetated parts of the continents, the regions where a large part of the human activity takes place. Radiative forcing by aerosol is also stronger for low surface albedo (e.g., water and vegetation). Therefore we

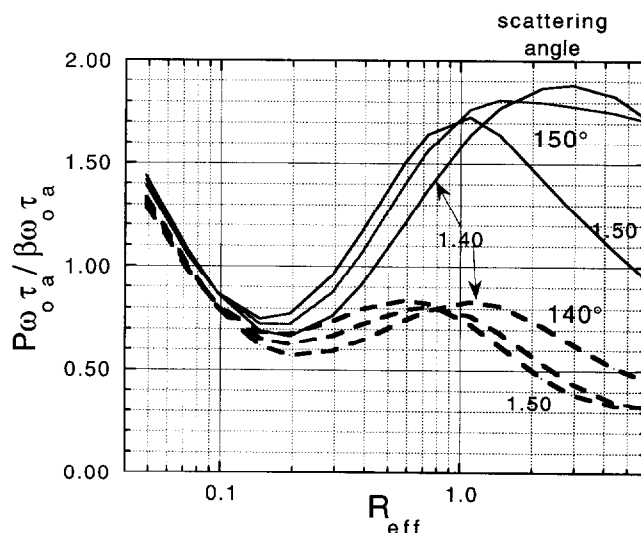


Figure 14. Effect of particle size on remote sensing of radiative forcing given by the ratio of the path radiance to the average radiative flux. For scattering angle of 140° (dashed lines), the dependence on the particle size is smaller than for 150° (solid lines). For particle size between 0.1 and $1 \mu\text{m}$ the ratio between the aerosol path radiance and the radiative flux varies around 0.7 ± 0.15 for a scattering angle of 140° .

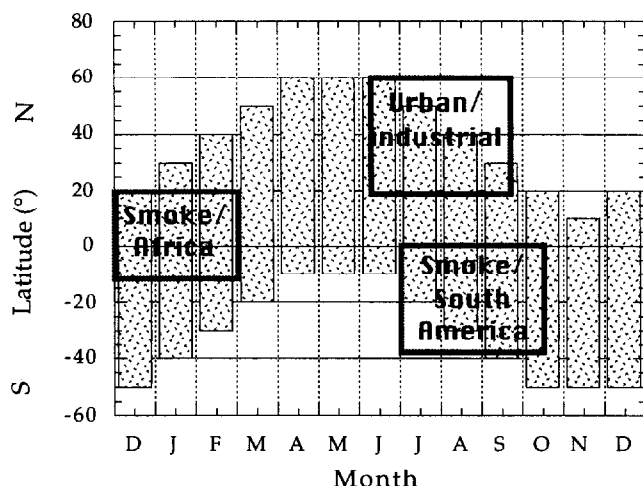


Figure 15. Coverage of latitudes for which a scattering angle of 150° can be derived, as a function of calendar month.

expect the algorithm to report aerosol loading and forcing in continental regions close to the main anthropogenic sources.

For efficient remote sensing of aerosol optical thickness over land and for estimation of the mass concentration and radiative forcing, several new remote sensing elements were developed and implemented: the use of mid-IR (2.1 and $3.8 \mu\text{m}$) to identify surface pixels that are dark in the red and blue channels and to estimate their reflectance; the use of dynamic aerosol models to describe the aerosol size distribution and scattering phase function (in these models the aerosol parameters depend on the optical thickness); and the use of weighted averages (rather than arithmetic averages) of aerosol climatology in order to derive the aerosol parameters for specific fixed scattering angles in order to minimize errors from uncertainty in the aerosol scattering phase function. The derivation of the optical thickness over the land will use a continuous validation procedure by updating periodically the algorithm by using aerosol properties derived from the AERONET global measurements. Substantial experience and validation was gained with the AVHRR $3.7 \mu\text{m}$ channel for identification of dense dark vegetation as the dark targets and with the Landsat TM and AVIRIS instruments for the $2.1 \mu\text{m}$ channel. Comprehensive evaluation of the $2.1 \mu\text{m}$ technique is still in progress. The main remaining uncertainties that were not addressed so far are the value of the refractive index and its possible variation with the optical thickness, the single-scattering albedo, and the aerosol nonsphericity. We hope to address them before the launch of the MODIS instrument.

The daily or twice a day (after the launch of the second EOS system in 2000) aerosol information over land and oceans (see Tanré *et al.* [this issue] for the ocean algorithm), combined with continuous detailed aerosol remote sensing of aerosol from the ground by AERONET and in situ measurements, will be used to study aerosol climatology, to monitor the sources and sinks of specific aerosol types, to study the interaction of aerosol with water vapor and clouds (both monitored by MODIS) and their radiative forcing of climate. It will also be used for atmospheric corrections of remotely sensed surface reflectance over the land [Tanré *et al.*, 1992; Running *et al.*, 1994; Vermote *et al.*, this issue]. For scattering angles around 150° the errors associated with the derived parameters are found to be minimum. The error in the derived aerosol mass of the accumulation

mode is smaller than that of the optical thickness of that mode. Radiative forcing can be derived with errors of $\pm 20\%$ even with a large uncertainty in the particle size (0.1 – $3 \mu\text{m}$). Detailed validation of the algorithm both before and after the EOS launch are planned to quantify the errors in different parts of the world and in order to continue and improve the algorithm.

Acknowledgments. We would like to thank S. Mattoo for writing the computer program for remote sensing of aerosol and R.-R. Li for the analysis of the data used for validation.

References

- Andreae, M. O., Climatic effects of changing atmospheric aerosol levels Ch 10, in *World Survey of Climatology*, vol. 16, *Future Climates of the World*, edited by A. Henderson-Sellers, pp. 341–392, Elsevier, New York, 1995.
- Andreae, M. O., Raising dust in the greenhouse, *Nature*, **380**, 389–390, 1996.
- Boucher, O., and T. L. Anderson, GCM assessment of the sensitivity of direct climate forcing by anthropogenic sulfate aerosols to aerosol size and chemistry, *J. Geophys. Res.*, **100**, 26,117–26,134, 1995.
- Bréon, F. M., J. L. Deuzé, D. Tanré, and M. Herman, Validation of spaceborne estimates of aerosol loading from Sun photometer measurements with emphasis on polarization, *J. Geophys. Res.*, this issue.
- Carlson, T. N., Atmospheric turbidity in Saharan dust outbreaks as determined by analyses of satellite brightness data, *Mon. Weather Rev.*, **107**, 322–335, 1979.
- Charlson, R. J., S. E. Schwartz, J. M. Hales, R. D. Cess, J. A. Coakley Jr., J. E. Hansen, and D. J. Hofman, Climate forcing of anthropogenic aerosols, *Science*, **255**, 423–430, 1992.
- Coakley, J. A., Jr., and R. D. Cess, Response of the NCAR community climate model to the radiative forcing by the naturally occurring tropospheric aerosols, *J. Atmos. Sci.*, **42**, 1677–1692, 1985.
- Coakley, J. A., Jr., R. L. Bernstein, and P. A. Durkee, Effect of ship stack effluents on cloud reflectance, *Science*, **237**, 953–1084, 1987.
- Crutzen, P. J., Atmospheric interaction-homogeneous gas reactions of C, N, and S containing compounds, pp. 67–114, in *The Major Biogeochemical Cycles and Their Interactions*, edited by B. Bolin and R. B. Cook, John Wiley, New York, 1983.
- Crutzen, P. J., and Andreae, M. O., Biomass burning in the tropics: Impact on atmospheric chemistry and biogeochemical cycles, *Science*, **250**, 1669–1678, 1990.
- d'Almeida, G. A., On the variability of desert aerosol radiative characteristics, *J. Geophys. Res.*, **92**, 3017–3026, 1987.
- d'Almeida, G. A., R. Jacnick, P. Roggendorf and D. Richter, New Sun photometer for network operation, *Appl. Opt.*, **22**(23), 3796–3801, 1983.
- d'Almeida, G. A., Koepke P., and E. P. Shettle, *Atmospheric Aerosols, Global Climatology and Radiative Characteristics*, A. Deepak, Hampton, Va., 1991.
- Deschamps, P. Y., F. M. Bréon, M. Leroy, A. Podaire, A. Bricaud, J. C. Buriez, and G. Sèze, The POLDER mission: Instrument characteristics and scientific objectives, *IEEE Trans. Geosci. Remote Sens.*, **32**, 598–615, 1994.
- Deuzé, J. L., F. M. Bréon, P. Y. Deschamps, C. Devaux, M. Herman, A. Podaire, and J. L. Roujean, Analysis of the POLDER (Polarization and Directionality of Earth's Reflectance): Airborne instrument observations over land surfaces, *Remote Sens. Environ.*, **44**, 151–168, 1993.
- Dulac, F., D. Tanré, G. Bergametti, P. Buat-Menard, M. Desbois, and D. Sutton, Assessment of the African airborne dust mass over the western Mediterranean Sea using Meteosat data, *J. Geophys. Res.*, **97**, 2489–2506, 1992.
- Durkee, P. A., F. Pfeil, E. Frost, and R. Shema, Global analysis of aerosol particle characteristics, *Atmos. Environ.*, **25**(A), 2457–2471, 1991.
- Flowers, E. C., R. A. McCormick, and K. R. Kurfis, Atmospheric turbidity over the United States, 1961–1966, *J. Appl. Meteorol.*, **8**, 955–962, 1969.
- Forgan, B. W., E. N. Rusina, J. J. DeLuise, and B. B. Hicks, Measurements of atmospheric turbidity in BAPMoN and looking forward to GAW, WMO Rep., World Meteorol. Organ., Geneva, 1994.

- Fraser, R. S., Satellite measurement of mass of Saharan dust in the atmosphere, *Appl. Opt.*, **15**, 2471–2479, 1976.
- Fraser, R. S., and Y. J. Kaufman, The relative importance of aerosol scattering and absorption in remote sensing, *IEEE J. Geosci. Remote Sens.*, **GE-23**, 525–633, 1985.
- Fraser, R. S., Y. J. Kaufman, and R. L. Mahoney, Satellite measurements of aerosol mass and transport, *Atmos. Environ.*, **18**, 2577–2584, 1984.
- Fraser, R. S., R. A. Ferrare, Y. J. Kaufman, and S. Mattoo, Algorithm for atmospheric corrections of aircraft and satellite imagery, *Int. J. Remote Sens.*, **13**, 541–557, 1992.
- Gao, B. C., and Y. J. Kaufman, Selection of the 1.375 μm MODIS channel for remote sensing of cirrus clouds and stratospheric aerosols from space, *J. Atmos. Sci.*, **52**, 4231–4237, 1995.
- Gao, B. C., K. B. Heidebrecht, and A. F. H. Goetz, Derivation of scaled surface reflectances from AVIRIS data, *Remote Sens. Environ.*, **44**, 165–178, 1993.
- Griggs, M., Measurements of atmospheric aerosol optical thickness over water using ERTS-1 data, *J. Air Pollut. Control Assoc.*, **25**, 622–626, 1975.
- Griggs, M., Satellite observations of atmospheric aerosols during the EOMET cruise, *J. Atmos. Sci.*, **36**, 695–698, 1979.
- Hao, W. M., and M. H. Liu, Spatial and temporal distribution of tropical biomass burning, *Global Biogeochem. Cycles*, **8**, 495–503, 1994.
- Hansen, J. E., and A. A. Lacis, Sun and dust versus greenhouse gases: An assessment of their relative roles in global climate change, *Nature*, **346**, 713–719, 1990.
- Hegg, D. A., P. V. Hobbs, R. J. Ferek, and A. P. Waggoner, Measurements of some aerosol properties relevant to radiative forcing on the east coast of the United States, *J. Appl. Meteorol.*, **34**, 2306–2315, 1995.
- Hobbs, P. V., J. S. Reid, J. A. Herring, J. D. Nance, R. E. Weiss, J. L. Ross, D. A. Hegg, R. D. Ottmar, and C. Lousise, Particle and trace gas measurements in the smoke from prescribed burns of forest products in the Pacific Northwest, in *Global Biomass Burning*, MIT Press, Cambridge, Mass., in press, 1996.
- Holben, B. N., T. F. Eck, and R. S. Fraser, Temporal and spatial variability of aerosol optical depth in the Sahel region in relation to vegetation remote sensing, *Int. Remote Sens.*, **12**, 1147–1163, 1991.
- Holben, B. N., E. Vermote, Y. J. Kaufman, D. Tanré, and V. Kalb, Aerosols retrieval over land from AVHRR data—Application for atmospheric correction, *IEEE Trans. Geosci. Remote Sens.*, **30**, 212–222, 1992.
- Holben, B. N., A. Setzer, T. F. Eck, A. Pereira, and I. Slutsker, Effect of dry season biomass burning on Amazon Basin aerosol concentrations and optical properties, 1992–1994, *J. Geophys. Res.*, **101**, 19,465–19,481, 1996.
- Hoppel, W. A., J. W. Fitzgerald, G. M. Frick, R. E. Larson, and E. J. Mack, Aerosol size distribution and optical properties found in the marine boundary layer over the Atlantic Ocean, *J. Geophys. Res.*, **95**, 3659–3686, 1990.
- Husar, R. B., J. Prospero, and L. L. Stowe, Characterization of tropospheric aerosols over the oceans with the NOAA/advanced very high resolution radiometer on remote sensing of optical thickness operational product, *J. Geophys. Res.*, this issue.
- Ignatov, A. M., L. L. Stowe, S. M. Sakerin, and G. K. Korotaev, Validation of the NOAA/NESDIS satellite aerosol product over the North Atlantic in 1989, *100*, 5123–5132, 1995.
- Intergovernmental Panel on Climate Change (IPCC), *Radiative Forcing of Climate Change*, Cambridge Univ. Press, New York, 1995.
- Jankowiak, I., and D. Tanré, Climatology of Saharan dust events observed from Meteosat imagery over Atlantic Ocean, Method and preliminary results, *J. Clim.*, **5**, 646–656, 1992.
- Jones, A., D. L. Roberts, and A. Slingo, A climate model study of indirect radiative forcing by anthropogenic sulphate aerosols, *Nature*, **370**, 450–453, 1994.
- Joseph, Y. A., The sensitivity of a numerical model of the global atmosphere to the presence of desert aerosol, in *Aerosols and Their Climatic Effects*, edited by H. E. Gerber and A. Deepak, pp. 215–226, A. Deepak, Hampton, Va., 1984.
- Kahn, R., R. West, D. McDonald, B. Rheingans, and M. I. Mishchenko, Sensitivity of multiangle remote sensing observations to aerosol sphericity, *J. Geophys. Res.*, this issue.
- Karl, T. R., R. W. Knight, G. Kukla, and J. Gavin, Evidence for radiative effects of anthropogenic sulfate aerosol in the observed climate record, in *Aerosol Forcing of Climate*, edited by R. J. Charlson and Heintzenberg, pp. 363–382, John Wiley, New York, 1995.
- Kaufman, Y. J., Satellite sensing of aerosol absorption, *J. Geophys. Res.*, **92**, 4307–4317, 1987.
- Kaufman, Y. J., Measurements of the aerosol optical thickness and the path radiance—Implications on aerosol remote sensing and atmospheric corrections, *J. Geophys. Res.*, **98**, 2677–2692, 1993.
- Kaufman, Y. J., Remote Sensing of the direct and indirect aerosol forcing, in *Aerosol Forcing of Climate*, edited by R. J. Charlson and Heintzenberg, pp. 298–332, John Wiley, New York, 1995.
- Kaufman, Y. J., R. S. Fraser, and R. A. Ferrare, Satellite measurements of large-scale air pollution methods, *J. Geophys. Res.*, **95**, 9895–9909, 1990a.
- Kaufman, Y. J., C. J. Tucker, and I. Fung, Remote sensing of biomass burning in the tropics, *J. Geophys. Res.*, **95**, 9927–9939, 1990b.
- Kaufman, Y. J., and B. N. Holben, Hemispherical backscattering by biomass burning and sulfate particles derived from sky measurements, *J. Geophys. Res.*, **101**, 19,433–19,445, 1996.
- Kaufman, Y. J., and T. Nakajima, Effect of Amazon smoke on cloud microphysics and albedo—Analysis from satellite imagery, *J. Appl. Meteorol.*, **32**, 729–744, 1993.
- Kaufman, Y. J., and L. Remer, Remote sensing of vegetation in the mid-IR: The 3.75 μm channels, *IEEE J. Geosci. Remote Sens.*, **32**, 672–683, 1994.
- Kaufman, Y. J., and C. Sendra, Algorithm for atmospheric corrections, *Int. J. Remote Sens.*, **9**, 1357–1381, 1988.
- Kaufman, Y. J., and D. Tanré, Variations in cloud supersaturation and the aerosol indirect effect on climate, *Nature*, **369**, 45–48, 1994.
- Kaufman, Y. J., and D. Tanré, Direct and indirect methods for correcting the aerosol effect on remote sensing, *Remote Sens. Environ.*, **55**, 65–79, 1996.
- Kaufman, Y. J., A. Gitelson, A. Karnieli, E. Ganor, R. S. Fraser, T. Nakajima, S. Mattoo, and B. N. Holben, Size distribution and phase function of aerosol particles retrieved from sky brightness measurements, *J. Geophys. Res.*, **99**, 10,341–10,356, 1994.
- Kaufman, Y. J., A. Setzer, D. Ward, D. Tanré, B. N. Holben, P. Menzel, M. C. Pereira, and R. Rasmussen, Biomass Burning Airborne and Spaceborne Experiment in the Amazonas (BASE A), *J. Geophys. Res.*, **97**, 14,581–14,599, 1992.
- Kaufman, Y. J., A. Wald, L. A. Remer, B.-C. Gao, R.-R. Li, and L. Flynn, Remote sensing of aerosol over the continents with the aid of a 2.2 μm channel, *IEEE Trans. Geosci. Remote Sens.*, in press, 1997.
- Kiehl, J. T., and B. P. Briegleb, The relative roles of sulfate aerosols and greenhouse gases in climate forcing, *Science*, **260**, 311–314, 1993.
- King, M. D., Determination of the ground albedo and the index of absorption of atmospheric particulates by remote sensing, II, Application, *J. Atmos. Sci.*, **36**, 1072–1083, 1979.
- King, M. D., D. M. Byrne, B. M. Herman, and J. A. Reagan, Aerosol size distribution obtained by inversion of optical depth measurements, *J. Atmos. Sci.*, **35**, 2153–2167, 1978.
- King, M. D., Y. Kaufman, P. Menzel, and D. Tanré, 1992, Remote sensing of cloud, aerosol and water vapor properties from the moderate resolution imaging spectrometer (MODIS), *IEEE Trans. Geosci. Remote Sens.*, **30**, 2–27, 1992.
- Koepke, P., and H. Quenzel, Turbidity of the atmosphere determined from satellite calculation of optimum viewing geometry, *J. Geophys. Res.*, **84**, 7847–7855, 1979.
- Langner, J., H. Rodhe, P. J. Crutzen, and P. Zimmermann, Anthropogenic influence on the distribution of tropospheric sulphate aerosol, *Nature*, **359**, 712–715, 1992.
- Lee, T., and Y. J. Kaufman, The effect of surface non-Lambertianity on remote sensing of ground reflectance and vegetation index, *IEEE J. Geosci. Remote Sens.*, **GE-24**, 699–708, 1986.
- Lenoble, J., and C. Brogniez, A comparative review of radiation aerosol model, *Beitr. Phys. Atmos.*, **57**(1), 1–20, 1984.
- Li, X., H. Maring, D. Savoie, K. Voss, and J. M. Prospero, Dominance of mineral dust in aerosol light scattering in the North Atlantic trade winds, *Nature*, **380**, 416–419, 1996.
- Liousse, C., J. E. Penner, C. Chuang, J. J. Walton, H. Eddleman, and H. Cachier, A global three-dimensional model study of carbonaceous aerosols, *J. Geophys. Res.*, **101**, 19,411–19,432, 1996.
- Martins, J. V., P. Artaxo, C. Liousse, H. Cachier, Y. Kaufman, and A. P. Fattori, Size distribution, elemental composition, carbon measurements and calculated optical properties of biomass burning

- aerosol particles during the SCAR-C experiment, in *Global Biomass Burning*, MIT Press, Cambridge, Mass., in press, 1996.
- Martonchik, J. V., and D. J. Diner, Retrieval of aerosol and land surface optical properties from multi-angle satellite imagery, *IEEE Trans. Geosci. Remote Sens.*, **30**, 223–230, 1992.
- Mekler, Y., H. Quenzel, G. Ohring, and I. Marcus, Relative atmospheric aerosol content from ERTS observations, *J. Geophys. Res.*, **82**, 967–972, 1977.
- Mishchenko, M. I., and L. D. Travis, Light scattering by polydispersions of randomly oriented spheroids with sizes comparable to wavelengths of observation, *Appl. Opt.*, **33**, 7206–7225, 1994.
- Nakajima, T., M. Tanaka, and T. Yamauchi, Retrieval of the optical properties of aerosols from aureole and extinction data, *Appl. Opt.*, **22**, 2951–2959, 1983.
- Nakajima, T., T. Takamura, M. Yamano, M. Shiobara, T. Yamauchi, R. Goto, and K. Murai, Consistency of aerosol size distribution inferred from measurements of solar radiation and aureole, *J. Meteorol. Soc. Jpn.*, **64**, 765–776, 1986.
- Nakajima, T., M. Tanaka, M. Yamano, M. Shiobara, K. Arao, and Y. Nakanishi, Aerosol optical characteristics in the yellow sand events observed in May, 1982 at Nagasaki, 2, Models, *J. Meteorol. Soc. Jpn.*, **67**, 279–291, 1989.
- Norton, C. C., F. R. Moshier, B. Hinton, D. W. Martin, D. Santek, and W. Kuhlman, A model for calculating desert aerosol turbidity over oceans from geostationary satellite data, *J. Appl. Meteorol.*, **19**, 633–642, 1980.
- Petterson, J. T., E. C. Flowers, G. J. Berri, C. L. Reynolds, and J. H. Rudisill, Atmospheric turbidity over central North Carolina, *J. Appl. Meteorol.*, **20**, 229–241, 1981.
- Penner, J. E., R. E. Dickinson, and C. A. O'Neill, Effects of aerosol from biomass burning on the global radiation budget, *Science*, **256**, 1432–1434, 1992.
- Prins, E. M., and W. P. Menzel, Trends in South American biomass burning detected with the GOES VISSR radiometer atmospheric sounder from 1983 to 1991, *J. Geophys. Res.*, **99**, 16,719–16,735, 1994.
- Prospero, J. M., Eolian transport to the world ocean, in *The Sea*, vol. 7, *The Oceanic Lithosphere*, edited by C. Emiliani, pp. 801–874, John Wiley, New York, 1981.
- Prospero, J. M., and R. T. Nees, Impact of the North African drought and El Niño on mineral dust in the Barbados trade wind, *Nature*, **320**, 735–738, 1986.
- Pye, K., *Eolian Dust and Dust Deposit*, 335 pp., Academic, San Diego, Calif., 1987.
- Radke, L. F., D. A. Hegg, P. V. Hobbs, J. D. Nance, J. H. Lyons, K. K. Laursen, P. J. Reagan, and D. E. Ward, Particulate and trace gas emission from large biomass fires in North America, in *Global Biomass Burning*, pp. 209–224, MIT Press, Cambridge, Mass., 1991.
- Rao, C. R. N., E. P. McClain, and L. L. Stowe, Remote-sensing of aerosols over the oceans using AVHRR data theory, practice and applications, *Int. J. Remote Sens.*, **10**, 743–749, 1989.
- Remer, L. A., Y. J. Kaufman, and B. N. Holben, The size distribution of ambient aerosol particles: Smoke vs. urban/industrial aerosol, in *Global Biomass Burning*, MIT Press, Cambridge, Mass., in press, 1996.
- Remer, L. A., S. Gassó, D. A. Hegg, Y. J. Kaufman, and B. N. Holben, Urban/industrial aerosol: Ground-based Sun/sky radiometer and airborne in situ measurements, *J. Geophys. Res.*, this issue.
- Roger, J. C., and E. F. Vermote, Computations and use of the reflectivity at 3.75 μm from AVHRR thermal channels, *Remote Sens. Environ.*, in press, 1997.
- Running, S. W., et al., Terrestrial remote sensing science and algorithms planned for EOS/MODIS, *Int. J. Remote Sens.*, **15**, 3587–3620, 1994.
- Salomonson, V. V., W. L. Barnes, P. W. Maymon, H. E. Montgomery, and H. Ostrow, MODIS: Advanced facility instrument for studies of the Earth as a system, *IEEE Trans. Geosci. Remote Sens.*, **27**, 145–153, 1989.
- Santer, B. D., et al., A search for human influence on the thermal structure of the atmosphere, *Nature*, **382**, 39–46, 1996.
- Shettle, E. P., Optical and radiative properties of a desert aerosol model, in *Proceedings of the Symposium on Radiation in the Atmosphere*, edited by G. Fiocco, pp. 74–77, A. Deepak, Hampton, Va., 1984.
- Shettle, E. P., and R. W. Fenn, Models for the aerosol of the lower atmosphere and the effect of humidity variations on their optical properties, *AFGL-TR790214*, Opt. Phys. Div., Air Force Geophys. Lab., Hanscom Air Force Base, Mass., 1979.
- Shiobara, M., T. Hayasaka, T. Nakajima, and M. Tanaka, Aerosol monitoring using a scanning spectral radiometer in Sendai, Japan, *J. Meteorol. Soc. Jpn.*, **69**, 57–70, 1991.
- Sokolik, I. N., and O. B. Toon, Direct radiative forcing by anthropogenic airborne mineral aerosol, *Nature*, **381**, 681–683, 1996.
- Soufflet, V., D. Tanré, and A. Royer, Remote sensing of aerosols over boreal forest and lake from AVHRR/NOAA data, *Remote Sens. Environ.*, in press, 1997.
- Tanré, D., J. F. Geleyn, and J. Slingo, First results of the introduction of an advanced aerosol-radiation interaction in ECMWF low resolution global model, in *Aerosols and Their Climatic Effects*, edited by H. E. Gerber and A. Deepak, pp. 133–177, A. Deepak, Hampton, Va., 1984.
- Tanré, D., P. Y. Deschamps, C. Devaux, and M. Herman, Estimation of Saharan aerosol optical thickness from blurring effects in Thematic Mapper data, *J. Geophys. Res.*, **93**, 15,955–15,964, 1988.
- Tanré, D., B. N. Holben, and Y. J. Kaufman, Atmospheric correction algorithm for NOAA-AVHRR products, theory and application, *IEEE J. Geosci. Remote Sens.*, **30**, 231–248, 1992.
- Tanré, D., Y. J. Kaufman, M. Herman, and S. Mattoo, Remote sensing of aerosol properties over oceans using EOS/MODIS spectral radiances, *J. Geophys. Res.*, this issue.
- Taylor, G. S., M. B. Baker, and R. J. Charlson, Heterogeneous interactions of the C, N and S cycles in the atmosphere: The role of aerosols and clouds, in *The Major Biogeochemical Cycles and Their Interactions*, edited by B. Bolin and R. B. Cook, John Wiley, New York, 1983.
- Tegen, I., A. A. Lacis, and I. Fung, The influence on climate forcing of mineral aerosols from disturbed soils, *Nature*, **380**, 419–422, 1996.
- Travis, L. D., EOSP: Earth Observing Scanning Polarimeter, in *EOS Reference Handbook 1993*, edited by G. Asrar and D. J. Dokken, pp. 74–75, NASA, 1993, 1993.
- Twomey, S. A., M. Piepgrass, and T. L. Wolfe, An assessment of the impact of pollution on the global albedo, *Tellus Ser. B.*, **36**, 356–366, 1984.
- Vermote, E. F., D. Tanré, J. L. Deuze, M. Herman, and J. Morcrette, Second Simulation of the Satellite Signal in the Solar Spectrum: An overview, *IEEE Trans. Geosci. Remote Sens.*, in press, 1996.
- Vermote, E., N. E. L. Saleous, C. Justice, Y. J. Kaufman, L. A. Remer, J. C. Roger, and D. Tanré, Atmospheric correction of visible to middle infrared EOS-MODIS data over land surface, background, operational algorithm and validation, *J. Geophys. Res.*, this issue.
- Volz, F., Himmelslicht und atmosphärische Trübung, *Wetter Leben*, **6**, 99–104, 1954.
- Wang, M., and H. R. Gordon, Retrieval of columnar aerosol phase function and single scattering albedo from sky radiance over the ocean: Simulations, *Appl. Opt.*, **32**, 4598–4609, 1993.
- Whitby, K. Y., The physical characteristics of sulfur aerosols, *Atmos. Environ.*, **12**, 135–159, 1978.
- World Meteorological Organization (WMO), Radiation commission of IAMAP meeting of experts on aerosol and their climatic effects, *WCP55*, Williamsburg, Va., 28–30 March, 1983.
- A. Chu and L. A. Remer, Science, Systems and Applications Inc., Code 913, NASA GSFC, Greenbelt, MD 20771.
- B. N. Holben, NASA Goddard Space Flight Center, Code 923, Greenbelt, MD 20771.
- Y. J. Kaufman, NASA Goddard Space Flight Center, Code 913, Greenbelt, MD 20771. (e-mail: kaufman@climate.gsfc.nasa.gov)
- D. Tanré, Laboratoire d'Optique Atmosphérique, Université de Sciences et Techniques de Lille, Villeneuve d'Ascq, France.
- E. F. Vermote, Department of Geography, University of Maryland and NASA Goddard SFC, Code 923, Greenbelt, MD 20771.

(Received February 7, 1996; revised November 6, 1996; accepted November 6, 1996.)